

---

# CMS Physics Analysis Summary

---

Contact: cms-pag-conveners-top@cern.ch

2018/11/19

Measurements of normalised multi-differential cross sections for top quark pair production in pp collisions at  $\sqrt{s} = 13$  TeV and simultaneous determination of the strong coupling strength, top quark pole mass and parton distribution functions

The CMS Collaboration

## Abstract

Normalised multi-differential cross sections for top quark pair ( $t\bar{t}$ ) production are measured in pp collisions at a centre-of-mass energy of 13 TeV using events containing two opposite-sign leptons. The analysed dataset was recorded by the CMS detector in 2016 and corresponds to an integrated luminosity of  $35.9 \text{ fb}^{-1}$ . The  $t\bar{t}$  cross section is measured double-differentially as a function of the kinematic properties of the top quark and the  $t\bar{t}$  system at parton level in the full phase space. A triple-differential measurement is performed as a function of the invariant mass and rapidity of the  $t\bar{t}$  system and the multiplicity of additional jets at particle level in the event. The data are compared to predictions of Monte Carlo event generators that complement next-to-leading-order (NLO) QCD calculations with parton showers. Together with a fixed order NLO QCD calculation the triple-differential measurement is used to extract values of the strong coupling strength ( $\alpha_s$ ) and the top quark pole mass ( $m_t^{\text{pole}}$ ) using several parton distribution function (PDF) sets. Furthermore, a simultaneous fit of PDFs,  $\alpha_s$  and  $m_t^{\text{pole}}$  is performed at NLO, demonstrating that the new data have significant impact on the gluon PDF and at the same time allow to accurately determine  $\alpha_s$  and  $m_t^{\text{pole}}$ .



## 1 Introduction

Measurements of the top quark pair ( $t\bar{t}$ ) production are essential for testing the standard model (SM) and searching for new phenomena. In particular, the large data set delivered by the CERN LHC allows us to make precise measurements of the  $t\bar{t}$  production differential cross section as a function of  $t\bar{t}$  kinematic observables. Such measurements test the most recent predictions of perturbative quantum chromodynamics (QCD) and can be used to constrain several input parameters, some of which are fundamental in the SM. At the LHC, top quarks are predominantly produced via gluon-gluon fusion. Thus, using measurements of the production cross section in a global fit of parton distribution functions (PDFs) can help to better determine the gluon distribution at large values of  $x$ , where  $x$  is the fraction of the proton momentum carried by a parton [1–3]. Furthermore, measurements of the cross section as a function of the  $t\bar{t}$  invariant mass, from the mass threshold to large values, provide high sensitivity for constraining the top quark pole mass,  $m_t^{\text{pole}}$ , which is defined as the pole of the top quark propagator. At LHC energies, the fraction of  $t\bar{t}$  events produced with additional hard jets in the final state is large. The processes with additional jets constitute important backgrounds for interesting rare SM processes such as associated production of a Higgs boson with  $t\bar{t}$  as well as for many new physics searches with  $t\bar{t}$  and thus need to be understood. Within the SM, processes with extra jets can be used to constrain the strength of the strong coupling at the scale of the top mass. Furthermore, the production of  $t\bar{t}$  in association with extra jets provides an additional sensitivity to  $m_t^{\text{pole}}$  since gluon radiation depends on  $m_t^{\text{pole}}$  through threshold and cone effects [4].

Differential cross sections for  $t\bar{t}$  production have been measured previously in proton-antiproton collisions at the Tevatron at a centre-of-mass energy of 1.96 TeV [5, 6] and in pp collisions at the LHC at  $\sqrt{s} = 7$  TeV [7–11], 8 TeV [11–17], and 13 TeV [18–23]. A recent milestone was achieved with the analyses [17, 19], where the  $t\bar{t}$  production dynamics was probed with double-differential cross sections. The analysis [17] used data recorded at  $\sqrt{s} = 8$  TeV by the CMS experiment in 2012. Only  $t\bar{t}$  decays were considered, where, after the decay of each top quark into a bottom quark and a W boson, both of the W bosons decay leptonically. Specifically the  $e^\pm\mu^\mp$  decay mode ( $e\mu$ ) was selected, requiring two oppositely-charged leptons and at least two jets. In this note a new measurement is presented, following the procedures from Ref. [17]. It is based on data taken by the CMS experiment in 2016 at  $\sqrt{s} = 13$  TeV, corresponding to an integrated luminosity of  $35.9 \pm 0.9 \text{ fb}^{-1}$ . In addition to  $e\mu$ , the two other dilepton decay modes  $e^+e^-$  ( $ee$ ) and  $\mu^+\mu^-$  ( $\mu\mu$ ) are also selected, roughly doubling the total number of expected  $t\bar{t}$  signal events. The present measurement complements the analysis [19] that is based on data from the same run period but selecting  $t\bar{t}$  decays into the  $\ell$ +jets ( $\ell = e, \mu$ ) final state.

As in the previous paper [17], measurements of the normalised double-differential  $t\bar{t}$  production cross section are performed. The cross section is measured as a function of observables describing the kinematics of the top quark and  $t\bar{t}$ : the transverse momentum of the top quark,  $p_T(t)$ , the rapidity of the top quark,  $y(t)$ , the transverse momentum,  $p_T(t\bar{t})$ , the rapidity,  $y(t\bar{t})$ , and the invariant mass,  $M(t\bar{t})$ , of  $t\bar{t}$ , the pseudorapidity difference between the top quark and antiquark,  $\Delta\eta(t, \bar{t})$ , and the angle between the top quark and antiquark in the transverse plane,  $\Delta\phi(t, \bar{t})$ . In total, the double-differential  $t\bar{t}$  cross section is measured as a function of six different pairs of kinematic variables. As demonstrated in Ref. [17], the different combinations of kinematic variables are sensitive to specific aspects of the SM theory calculations.

In this note, for the first time, the triple-differential cross section is measured as a function of  $M(t\bar{t})$ ,  $y(t\bar{t})$  and  $N_{\text{jet}}$ , where  $N_{\text{jet}}$  is the number of extra jets not coming from the decay of the  $t\bar{t}$  system. For this purpose the kinematic reconstruction algorithm is optimised to determine the invariant mass of the  $t\bar{t}$  system in an unbiased way. As will be shown below, the triple-

differential measurements provide tight constraints on the parametrised gluon distribution in the proton, the strong coupling strength, and the top quark pole mass. Previous studies of additional jet activity in  $t\bar{t}$  events at the LHC can be found in Refs. [19, 24, 25]. The strong coupling strength and the top quark pole mass were also extracted from measurements of the total inclusive  $t\bar{t}$  production cross sections in Refs. [26–31].

The measurements are defined at parton level and thus are corrected for the effects of hadronisation and detector resolutions and inefficiencies. A regularised unfolding process is performed simultaneously in bins of the two or three variables in which the cross sections are measured. The normalised differential  $t\bar{t}$  cross section is determined by dividing the distributions with the measured total inclusive  $t\bar{t}$  production cross section, where the latter is evaluated by integrating over all bins in the respective observables.

The parton level results are compared with theoretical predictions obtained with the generators POWHEG (v. 2) [32, 33] and MG5\_aMC@NLO [34], interfaced to PYTHIA8 [35, 36] for parton showering, hadronisation, and multiple-parton interactions. They are also compared to theoretical predictions obtained at next-to-leading-order (NLO) QCD with several PDF sets, after applying corrections for non-perturbative effects.

The structure of the note is as follows: details of the event simulation are given in Section 2. The event selection, kinematic reconstruction, and comparisons between data and simulation are described in Section 3. The unfolding procedure is detailed in Section 4; the method to determine the differential cross sections is presented in Section 5, and the assessment of the systematic uncertainties is elucidated in Section 6. The results of the measurement are discussed and compared to theoretical predictions in Section 7. Section 8 presents the extraction of the strong coupling strength  $\alpha_s$  and top quark pole mass  $m_t^{\text{pole}}$  from the measured  $t\bar{t}$  cross sections using PDF sets, and Section 9 presents the simultaneous fit of PDFs,  $\alpha_s$  and  $m_t^{\text{pole}}$ . Finally, Section 10 provides a summary.

## 2 Event simulation

Simulations of physics processes are performed with Monte Carlo (MC) event generators and serve three purposes: firstly, to obtain representative SM predictions of  $t\bar{t}$  production cross sections to be compared to the results of this analysis. Secondly, when interfacing generated  $t\bar{t}$  signal events to a detector simulation, to determine corrections for the effects of reconstruction and selection efficiencies and resolutions that are to be applied to the data. Thirdly, when interfacing generated background processes to the detector simulation to obtain predictions for the backgrounds. All MC programs used in this analysis perform the event generation in three subsequent steps: matrix-element (ME) level, parton showering matched to ME, and hadronisation. The  $t\bar{t}$  signal processes are simulated with ME calculations at NLO in QCD. For all simulations the proton structure is described by the NNPDF3.0\_nlo\_as\_0118 [37] PDF set and the value of the top quark mass is fixed to  $m_t = 172.5 \text{ GeV}$ . For the default signal simulation the POWHEG (v. 2) [32, 38, 39] generator (POWHEGV2) is taken. The  $h_{\text{damp}}$  parameter of POWHEGV2, which regulates the damping of real emissions in the NLO calculation when matching to the parton shower, is set to  $h_{\text{damp}} = 1.581 m_t$ . The PYTHIA program (version 8.2) [36] with the CUETP8M2T4 tune [40–42], (PYTHIA8), is used to model parton showering, hadronisation and multiple-parton interactions. An alternative sample is generated using the MG5\_aMC@NLO (v. 2.2.2) [34] generator including up to two extra partons at the ME level with NLO precision. In this setup, referred to as MG5\_aMC@NLO + PYTHIA8 [FxFx], MADSPIN [43] is used to model the decays of the top quarks while preserving their spin correlation.

The events are matched to PYTHIA8 using the FxFx prescription [44]. A second alternative sample is generated with POWHEGV2 and interfaced with HERWIG++ (v. 2.7.1) [45] and the EE5C tune [46].

The main background contributions originate from single top quarks produced in association with a W boson (tW),  $Z/\gamma^*$  bosons produced with additional jets (Z+jets), W boson production with additional jets (W+jets) and diboson (WW, WZ, and ZZ) events. Other backgrounds are negligible. For all background samples, the NNPDF3.0 [37] PDF set is used and parton showering, hadronisation and multiple-parton interactions are simulated with PYTHIA8. Single top quark production is simulated with POWHEG (v. 1) [33, 47] using the CUETP8M2T4 tune in PYTHIA8 with the  $h_{\text{damp}}$  parameter set to 172.5 GeV in POWHEG. The Z+jets process is simulated at NLO precision using MG5\_aMC@NLO with up to two additional partons at ME level and matched to PYTHIA8 using the FxFx prescription. The W+jets process is simulated at leading-order (LO) precision using MG5\_aMC@NLO with up to four additional partons at ME level and matched to PYTHIA8 using the MLM prescription [48]. Diboson events are simulated with PYTHIA8. Predictions are normalised based on their theoretical cross sections and the integrated luminosity of the data. The cross sections are calculated at the highest orders of perturbative QCD currently available. This corresponds to approximate NNLO for single top quark in the tW channel [49], next-to-NLO (NNLO) for Z+jets and W+jets [50] and NLO calculations for diboson [51]. The  $t\bar{t}$  simulation is normalised to a cross section of  $831.76 \pm_{29.20}^{19.77}$  (scale)  $\pm 35.06$  (PDF +  $\alpha_s$ ) pb calculated with the TOP++2.0 program [52] at NNLO including resummation of next-to-next-to-leading-logarithm soft-gluon terms assuming a top-quark mass  $m_t^{\text{pole}} = 172.5$  GeV.

In all cases, the interactions of particles with the CMS detector is simulated using GEANT4 (v. 9.4) [53].

### 3 Event selection and $t\bar{t}$ kinematic reconstruction

The event selection procedure follows closely the one reported in Ref. [23]. Events are selected that correspond to the decay topology where both top quarks decay into a W boson and a b quark, and each of the W bosons decays into a muon or an electron and a neutrino. Three distinct final state channels are defined: the same-flavour channels corresponding to two muons ( $\mu^+\mu^-$ ) or two electrons ( $e^+e^-$ ) and the different-flavour channel corresponding to one electron and one muon ( $\mu^\pm e^\mp$ ). Final results are derived by combining the three channels. At HLT level, events are selected either by single-lepton or dilepton triggers. The former require the presence of at least one electron or muon and the latter the presence of either two electrons, two muons, or an electron and a muon. For the single-electron and single-muon triggers, transverse momentum  $p_T$  thresholds of 27 and 24 GeV are applied, respectively. The same-flavour dilepton triggers require either an electron pair with  $p_T > 23$  (12) GeV for the leading (sub-leading) electron or a muon pair with  $p_T > 17$  (8) GeV for the leading (sub-leading) muon, where leading (sub-leading) refers to the electron or muon with the highest (second highest)  $p_T$  in the event. The different-flavour dilepton triggers require either a muon with  $p_T > 23$  GeV and an electron with  $p_T > 12$  GeV, or an electron with  $p_T > 23$  GeV and a muon with  $p_T > 8$  GeV.

Events are reconstructed using a particle-flow algorithm [54], where each individual particle observed in pp collisions is identified and reconstructed with an optimised combination of information from the various elements of the CMS detector. Charged hadrons from additional pp interactions in the same or nearby beam crossings (pileup) are subtracted on an event-by-event basis. Subsequently, the remaining neutral-hadron component from pileup is accounted

for through jet energy corrections [55].

Electron candidates are reconstructed from a combination of the track momentum at the main interaction vertex, the corresponding energy deposition in the ECAL, and the energy sum of all bremsstrahlung photons associated with the track [56]. The electron candidates are required to have  $p_T > 25$  (20) GeV for the leading (sub-leading) candidates and  $|\eta| < 2.4$ . Electron candidates with ECAL clusters in the region between the barrel and endcap ( $1.4442 < |\eta_{\text{cluster}}| < 1.5660$ ) are excluded. A relative isolation criterion  $I_{\text{rel}} < 0.0588$  or  $< 0.0571$  is applied, depending on whether the electron candidate is reconstructed in the barrel or in the endcap. Here  $I_{\text{rel}}$  is defined as the sum of the  $p_T$  of all neutral hadron, charged hadron, and photon candidates within a distance of 0.3 from the electron in  $\eta - \phi$  space, divided by the  $p_T$  of the electron candidate. In addition, electron identification requirements are applied to reject misidentified electron candidates and candidates originating from photon conversions. Muon candidates are reconstructed using the track information from the tracker and the muon system. They are required to have  $p_T > 25$  (20) GeV for the leading (sub-leading) candidates and  $|\eta| < 2.4$ . An isolation requirement of  $I_{\text{rel}} < 0.15$  is applied to muon candidates including particles within a distance of 0.4 from the muon in  $\eta - \phi$  space. In addition, muon identification requirements are applied to reject misidentified muon candidates and candidates originating from in-flight decay processes. For both electron and muon candidates, a correction is applied to  $I_{\text{rel}}$  to suppress residual pileup effects.

Jets are reconstructed by clustering the particle-flow candidates using the anti- $k_T$  clustering algorithm [57, 58] with a distance parameter  $R = 0.4$ . To correct for the detector response,  $p_T$ - and  $\eta$ -dependent jet energy corrections are applied [59]. A jet is selected if it has  $p_T > 30$  GeV and  $|\eta| < 2.4$ . Jets are rejected if the distance in  $\eta - \phi$  space between the jet and the closest lepton,  $\Delta R(\text{jet}, \text{lepton})$ , is less than 0.4. Jets originating from the hadronisation of b quarks (b jets) are identified with an algorithm [60] that is using secondary vertices together with track-based lifetime information to construct a b-tagging discriminant. The chosen working point has a b jet tagging efficiency of  $\approx 79\text{--}87\%$  and a mistagging efficiency of  $\approx 10\%$  for jets originating from gluons, as well as u, d, or s quarks, and  $\approx 30\text{--}40\%$  for jets originating from c quarks.

The missing transverse momentum vector  $\vec{p}_T^{\text{miss}}$  is defined as the projection on the plane perpendicular to the beams of the negative vector sum of the momenta of all PF particles in an event. Its magnitude is referred to as  $p_T^{\text{miss}}$ . Jet energy corrections are propagated to improve the determination of  $\vec{p}_T^{\text{miss}}$ .

Only  $t\bar{t}$  events with two electrons or muons that do not originate from the decays of tau leptons are considered as signal with all other  $t\bar{t}$  events regarded as background. Events are selected offline if they contain exactly two isolated electrons or muons of opposite electric charge. Furthermore they need to contain at least two jets and at least one of these jets must be b-tagged. Events with an invariant mass of the lepton pair,  $M(\ell\ell)$ , smaller than 20 GeV are removed in order to suppress contributions from heavy-flavour resonance decays and low-mass Drell-Yan processes. Backgrounds from Z+jets processes in the  $\mu^+\mu^-$  and  $e^+e^-$  channels are further suppressed by requiring  $|m_Z - M(\ell\ell)| > 15$  GeV where  $m_Z = 91$  GeV [61], and  $p_T^{\text{miss}} > 40$  GeV. The remaining background contribution from  $tW$ ,  $Z + \text{jets}$ ,  $W + \text{jets}$ , diboson and  $t\bar{t}$  events from decay channels other than that of the signal are estimated from the simulation.

In this analysis the  $t\bar{t}$  production cross section is also measured as a function of the extra jet multiplicity,  $N_{\text{jet}}$ . Extra jets (also referred to as additional jets) are jets arising primarily from hard QCD radiation and not from the top quark decays. At generator level the extra jets are defined in dilepton  $t\bar{t}$  events as jets with  $p_T > 30$  GeV,  $|\eta| < 2.4$  built of particles except neutrinos using the anti- $k_T$  clustering algorithm [57, 58] with a distance parameter  $R = 0.4$  and isolated

from the charged leptons (i.e.  $\mu$  or  $e$ ) and  $b$  quarks originating from the top quark decays by a minimal distance of 0.4 in  $\eta - \phi$  space. The charged leptons and  $b$  quarks are taken directly after  $W$  and top quark decays, respectively. At reconstruction level the extra jets are defined in dilepton  $t\bar{t}$  candidate events as jets with  $p_T > 30$  GeV,  $|\eta| < 2.4$  and isolated from the leptons and  $b$  jets originating from the top quark decays by the same minimal distance in  $\eta - \phi$  space.

The  $t\bar{t}$  kinematic properties are determined from the four-momenta of the decay products using a kinematic reconstruction method [12]. The three-momenta of the two neutrinos are not directly measured, but they can be reconstructed by imposing the following six kinematic constraints:  $p_T$  conservation in the event and the masses of the  $W$  bosons, top quark, and top antiquark. The reconstructed top quark and antiquark masses are required to be 172.5 GeV. The  $p_T^{\text{miss}}$  in the event is assumed to originate solely from the two neutrinos in the top quark and antiquark decay chains. To resolve the ambiguity due to multiple algebraic solutions of the equations for the neutrino momenta, the solution with the smallest invariant mass of the  $t\bar{t}$  system is taken. The reconstruction is performed 100 times, each time randomly smearing the measured energies and directions of the reconstructed leptons and jets within their resolution. This smearing procedure recovers certain events that initially yield no solution because of measurement errors. The three-momenta of the two neutrinos are determined as a weighted average over all smeared solutions. For each solution, the weight is calculated based on the expected invariant mass spectrum of a lepton and a bottom jet as the product of two weights for the top quark and antiquark decay chains. All possible lepton-jet combinations in the event that satisfy the requirement on the invariant mass of the lepton and jet  $M_{\ell b} < 180$  GeV are considered. Combinations are ranked based on the presence of  $b$ -tagged jets in the assignments, i.e. a combination with both leptons assigned to  $b$ -tagged jets is preferred over those with one or no  $b$ -tagged jet. Among assignments with equal number of  $b$ -tagged jets, the one with the highest sum of weights is chosen. Events with no solution after smearing are discarded. The efficiency of the kinematic reconstruction, defined as the number of events where a solution is found divided by the total number of selected  $t\bar{t}$  events, is studied in data and simulation and consistent results are observed. The efficiency is about 90% for signal events. After applying the full event selection and the kinematic reconstruction of the  $t\bar{t}$  system, 150 410 events are observed in the  $\mu^\pm e^\mp$  channel, 70 346 events in the  $\mu^+ \mu^-$  channel, and 34 890 events in the  $e^+ e^-$  channel. Combining all decay channels, the estimated signal fraction in data is 80.6%. Figure 1 shows the distributions of the reconstructed top quark and  $t\bar{t}$  kinematic variables and of the multiplicity of additional jets in the events. In general, the data are reasonably well described by the simulation, however some trends are visible, in particular for  $p_T(t)$ , where the simulation predicts a somewhat harder spectrum.

The  $M(t\bar{t})$  value obtained using the full kinematic reconstruction described above is highly sensitive to the value of the top mass used as a kinematic constraint. Since one of the objectives of this analysis is to extract the top quark mass from the differential  $t\bar{t}$  measurements, exploiting the  $M(t\bar{t})$  distribution in particular, an alternative algorithm is employed which reconstructs the  $t\bar{t}$  kinematics without using the top mass constraint. This algorithm is referred to as the “loose kinematic reconstruction”. In this algorithm, the total  $\nu\bar{\nu}$  system is reconstructed rather than the  $\nu$  and  $\bar{\nu}$  separately. Consequently, it can only be used to reconstruct the total  $t\bar{t}$  system but not the top quark and antiquark separately. As in the full kinematic reconstruction, all possible lepton-jet combinations in the event that satisfy the requirement on the invariant mass of the lepton and jet  $M_{\ell b} < 180$  GeV are considered. Combinations are ranked based on the presence of  $b$ -tagged jets in the assignments, but among combinations with equal number of  $b$ -tagged jets, the ones with the highest  $p_T$  jets are chosen. The kinematics of the  $\nu\bar{\nu}$  system is derived as follows: its transverse momentum is set equal to  $p_T^{\text{miss}}$ , while its unknown lon-

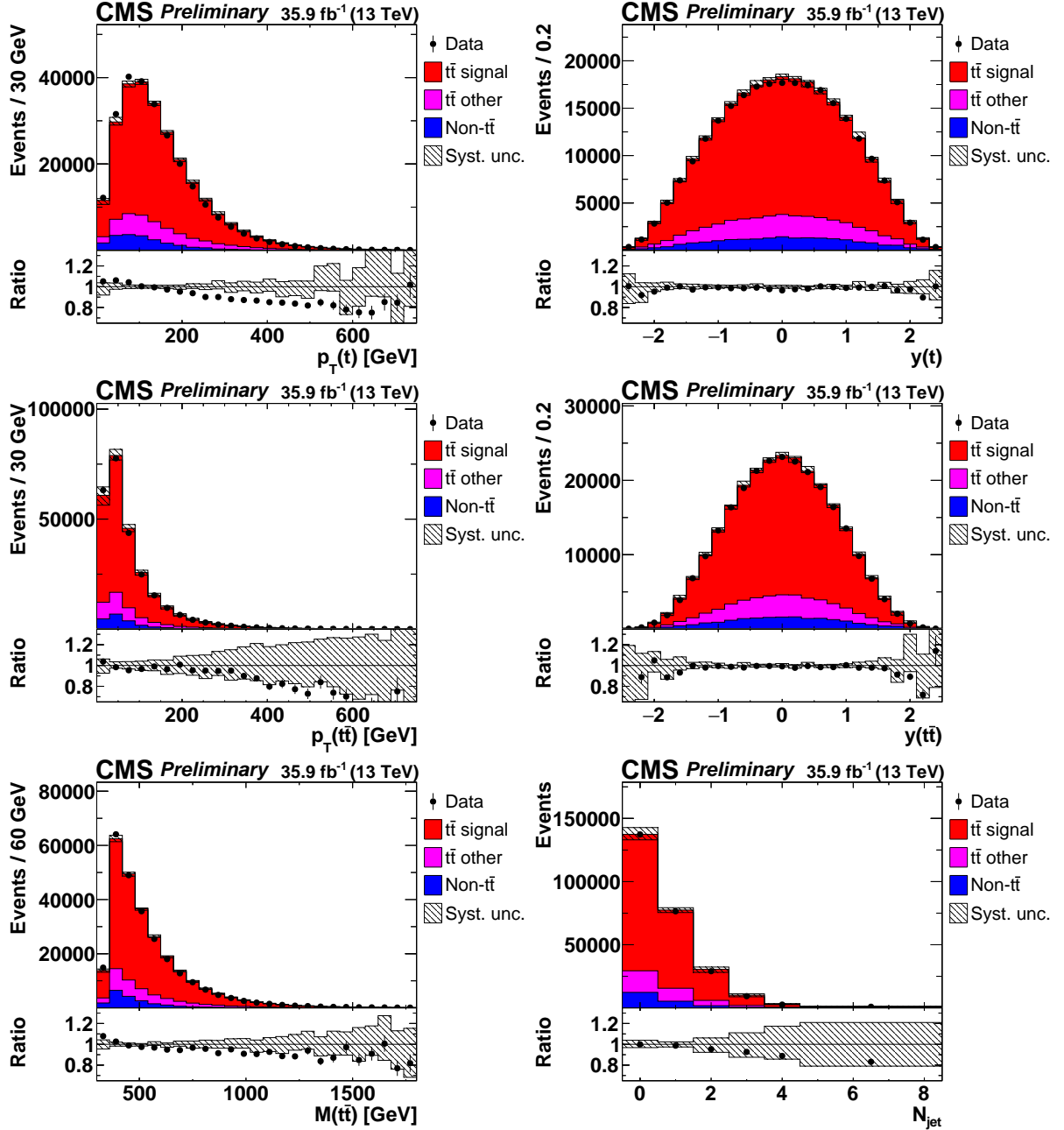


Figure 1: Distributions of  $p_T(t)$  (upper left),  $y(t)$  (upper right),  $p_T(t\bar{t})$  (middle left),  $y(t\bar{t})$  (middle right),  $M(t\bar{t})$  (lower left) and multiplicity of additional jets (lower right) in selected events after the kinematic reconstruction, at detector level. The experimental data with the vertical bars corresponding to their statistical uncertainties are plotted together with distributions of simulated signal and different background processes. The hatched regions correspond to the estimated shape uncertainties in the signal and backgrounds (see Section 6). The lower panel in each plot shows the ratio of the observed data event yields to those expected in the simulation.



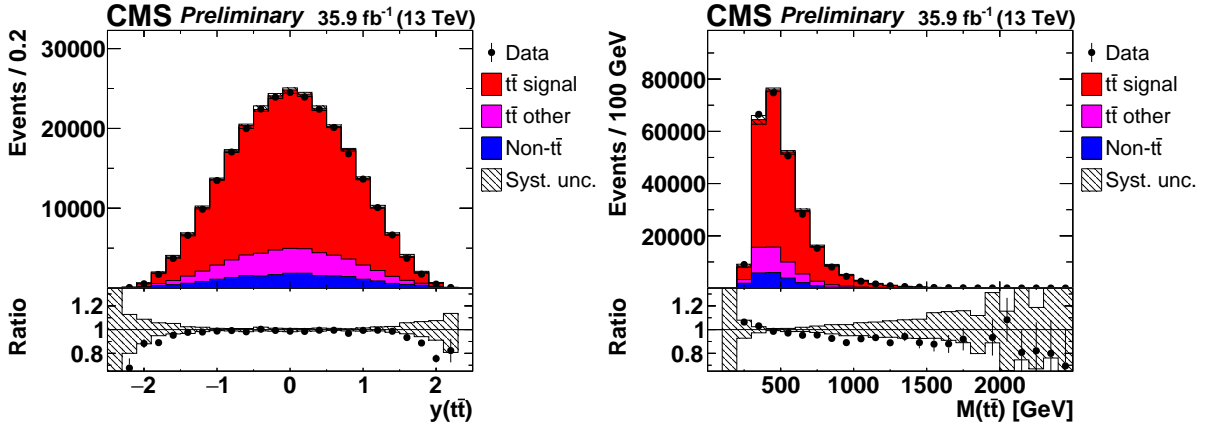


Figure 2: Distributions of  $y(t\bar{t})$  (left) and  $M(t\bar{t})$  (right) in selected events after the loose kinematic reconstruction. Details can be found in the caption of Fig. 1.

gitudinal momentum and energy are set equal to the longitudinal momentum and energy of the lepton pair. Additional constraints are applied on the invariant mass of the neutrino pair,  $M(\nu\bar{\nu}) \geq 0$ , and on the invariant mass of the W bosons,  $M(W^+W^-) \geq 2M_W$ , which have only minor effects on the performance of the reconstruction. The method yields similar  $t\bar{t}$  kinematic resolutions and reconstruction efficiency as for the full kinematic reconstruction. In this analysis, the loose kinematic reconstruction is exclusively used to measure triple-differential cross sections as a function of  $M(t\bar{t})$ ,  $y(t\bar{t})$  and extra jet multiplicity which are exploited to determine QCD parameters. Figure 2 shows the distributions of the reconstructed  $t\bar{t}$  invariant mass and rapidity using the loose kinematic reconstruction. These distributions are similar to the ones obtained using the full kinematic reconstruction (see Fig. 1).

## 4 Signal extraction and unfolding

The number of signal events in the data is extracted by subtracting the expected number of background events from the observed number of events for each bin of the observables. All expected background numbers are obtained directly from the MC simulations (see Section 2) except for  $t\bar{t}$  final states other than the signal. The latter are dominated by events in which one or both of the intermediate W bosons decay into  $\tau$  leptons with subsequent decay into an electron or muon. These events arise from the same  $t\bar{t}$  production process as the signal and thus the normalisation of this background is fixed to that of the signal. For each bin the number of events obtained after the subtraction of other background sources is multiplied by the ratio of the number of selected  $t\bar{t}$  signal events to the total number of selected  $t\bar{t}$  events (i.e. the signal and all other  $t\bar{t}$  events) in simulation.

The numbers of signal events obtained after background subtraction are corrected for detector effects, using the TUnfold package [62]. The response matrix plays a key role in this unfolding procedure. An element of this matrix specifies the probability for an event originating from one bin of the true distribution to be observed in a specific bin of the reconstructed observables. The response matrix includes the effects of the acceptance, detector efficiencies and resolutions. The response matrix is defined such that the true level corresponds to the full phase space (with no kinematic restrictions) for  $t\bar{t}$  production at parton level. At the detector level a binning is chosen in the same kinematic ranges as at the true level, but with the total number of bins typically a few times larger. The response matrix is taken from the signal simulation. The generalised inverse of the response matrix is used to obtain the distribution of unfolded event numbers

from the measured distribution by applying a  $\chi^2$  minimization technique. An additional  $\chi^2$  term is included representing Tikhonov regularization [63]. The regularization reduces the effect of the statistical fluctuations present in the measured distribution on the high-frequency content of the unfolded spectrum. The regularization strength is chosen such that the global correlation coefficient is minimal [64]. For the measurements presented here, this choice results in a small contribution from the regularization term to the total  $\chi^2$ , on the order of a few percent. The unfolding of multidimensional distributions is performed by internally mapping the multi-dimensional arrays to one-dimensional arrays [62].

## 5 Cross section determination

The normalised cross sections for  $t\bar{t}$  production are measured in the full  $t\bar{t}$  kinematic phase space at parton level. The number of unfolded signal events  $\hat{M}_i^{\text{unf}}$  in bins  $i$  of kinematic variables is used to define the normalised cross sections as a function of several (two or three) variables

$$\frac{\sigma_i}{\sigma} = \frac{1}{\sigma} \frac{\hat{M}_i^{\text{unf}}}{\mathcal{B} \mathcal{L}}, \quad (1)$$

where  $\sigma$  is the total cross section, which is evaluated by summing  $\sigma_i$  over all bins. For presentation purposes, the measured cross sections are divided by the bin width of the first variable. They present single-differential cross sections as a function of the first variable in different ranges of the second or second and third variables and are referred to as double- or triple-differential cross sections, respectively. The branching fraction of  $t\bar{t}$  into  $ee$ ,  $e\mu$  and  $\mu\mu$  final states is taken to be  $\mathcal{B} = 10.5\%$  [65], and  $\mathcal{L}$  is the integrated luminosity of the data sample. The bin widths are chosen based on the resolutions of the kinematic variables, such that the purity and the stability of each bin is generally above 20%. For a given bin, the purity is defined as the fraction of events in the  $t\bar{t}$  signal simulation that are generated and reconstructed in the same bin with respect to the total number of events reconstructed in that bin. To evaluate the stability, the number of events in the  $t\bar{t}$  signal simulation that are generated and reconstructed in a given bin are divided by the total number of reconstructed events generated in the bin.

## 6 Systematic uncertainties

The systematic uncertainties in the measured differential cross sections are categorised into two classes: experimental uncertainties arising from imperfect modelling of the detector response and theoretical uncertainties arising from the modelling of the signal and background processes. Each source of systematic uncertainty is assessed by changing in the simulation the corresponding efficiency, resolution, or scale by its uncertainty, using a prescription similar to the one followed in Ref. [23]. For each change made, the cross section determination is repeated, and the difference with respect to the nominal result in each bin is taken as the systematic uncertainty.

### 6.1 Experimental uncertainties

To account for the pileup uncertainty, the value of the total pp inelastic cross section, which is used to estimate the mean number of additional pp interactions, is varied by  $\pm 4.6\%$ , corresponding to the uncertainty in the measurement of this cross section presented in Ref. [66].

The efficiencies of the dilepton triggers are measured with independent triggers based on a  $p_T^{\text{miss}}$  requirement. Scale factors, defined as the ratio of the trigger efficiencies in data and simulation, are calculated in bins of lepton  $\eta$  and  $p_T$ . They are applied to the simulation and

varied within their uncertainties. The uncertainties from modelling of lepton identification and isolation efficiencies are determined using the tag-and-probe method with Z+jets event samples [67, 68]. The differences of these efficiencies between data and simulation in bins of  $\eta$  and  $p_T$  are generally less than 10% for electrons, and negligible for muons. An uncertainty is estimated by varying the corresponding MC scale factors within their uncertainties.

The uncertainty arising from the jet energy scale (JES) is determined by varying the twenty-six sources of uncertainty in the JES in bins of  $p_T$  and  $\eta$  and taking the quadrature sum of the effects [69]. The JES variations are also propagated to the uncertainties in  $p_T^{\text{miss}}$ . The uncertainty from the jet energy resolution (JER) is determined by the variation of the simulated JER by  $\pm 1$  standard deviation in different  $\eta$  regions [69]. An additional uncertainty from the calculation of  $p_T^{\text{miss}}$  is estimated by varying the energies of reconstructed particles not clustered into jets.

The uncertainty due to imperfect modelling of the b tagging efficiency is determined by varying the measured scale factor for b tagging efficiencies within its uncertainties.

The uncertainty in the integrated luminosity of the 2016 data sample recorded by CMS is 2.5% [70] and is applied to the normalisation of all simulated distributions coherently.

## 6.2 Theoretical uncertainties

The uncertainty arising from missing higher-order terms in the simulation of the signal process at ME level is assessed by varying the renormalisation and factorisation scales in the POWHEGV2 simulation up and down by factors of two with respect to the nominal values. In the POWHEGV2 sample, the nominal scales are defined as  $m_t^2 + p_{T,t}^2$ , where  $p_{T,t}$  denotes the  $p_T$  of the top quark in the  $t\bar{t}$  rest frame. In total, three variations are applied: one with the factorisation scale fixed, one with the renormalisation scale fixed, and one with both scales varied up and down coherently together. The maximum of the resulting measurement variations is taken as final uncertainty. In the parton-shower simulation, the corresponding uncertainty is estimated by varying the scale of initial- and final-state radiation separately up and down by factors of 2 and  $\sqrt{2}$  as suggested in Ref. [42].

The uncertainty from the choice of PDF is assessed by reweighting the signal simulation according to the prescription provided for the CT14 NNLO set [71]. An additional uncertainty is independently derived by varying the  $\alpha_s$  value within its uncertainty in the PDF set. The dependence of the measurement on the assumed top quark mass  $m_t$  value is estimated by varying  $m_t$  in the simulation by  $\pm 1$  GeV around the central value of 172.5 GeV.

The uncertainty originating from the scheme used to match the ME-level calculation to the parton-shower simulation is derived by varying the  $h_{\text{damp}}$  parameter in POWHEGV2 in the range  $0.996m_t < h_{\text{damp}} < 2.239m_t$ , according to the tuning results from Ref. [40].

The uncertainty related to modelling of the underlying event is estimated by varying the parameters used to derive the CUETP8M2T4 tune in the default setup. The default setup in PYTHIA8 includes an MPI-based model of colour reconnection with early resonance decays switched off. The analysis is repeated with three other models of colour reconnection within PYTHIA8: the MPI-based scheme with early resonance decays switched on, a gluon-move scheme [72], and a QCD-inspired scheme [73]. The total uncertainty from colour reconnection modelling is estimated by taking the maximum deviation from the nominal result.

The uncertainty from the knowledge of the b quark fragmentation function is assessed by varying the Bowler-Lund function within its uncertainties [74]. In addition, the analysis is repeated using the Peterson model for b quark fragmentation [75]. An uncertainty from the semileptonic

branching ratio of  $b$  hadrons is estimated by correcting the  $t\bar{t}$  simulation to match the branching ratio in Ref. [61]. As  $t\bar{t}$  events producing electrons or muons originating from the decay of tau leptons are considered to be background, the measured differential cross sections are sensitive to the branching ratios of tau leptons decaying into electrons or muons assumed in the simulation. Hence, an uncertainty is determined by varying the branching ratios by 1.5% [61] in the simulation.

The normalisations of all non- $t\bar{t}$  backgrounds are varied up and down by  $\pm 30\%$  taken from measurements as explained in Ref. [68].

The total systematic uncertainty in each measurement bin is estimated by adding all the contributions described above in quadrature, separately for positive and negative cross section variations. If a systematic uncertainty results in two cross section variations of the same sign, the largest one is taken, while the opposite variation is set to zero.

## 7 Results of the measurement

The normalised differential cross sections for  $t\bar{t}$  production are measured in the full phase space at parton level (after radiation and before the top quark and antiquark decays) for the following variables:

1. double-differential cross sections as a function of pair of variables:

- $y(t)$  and  $p_T(t)$ ,
- $M(t\bar{t})$  and  $y(t)$ ,
- $M(t\bar{t})$  and  $y(t\bar{t})$ ,
- $M(t\bar{t})$  and  $\Delta\eta(t, \bar{t})$ ,
- $M(t\bar{t})$  and  $\Delta\phi(t, \bar{t})$ ,
- $M(t\bar{t})$  and  $p_T(t\bar{t})$ ,
- $M(t\bar{t})$  and  $p_T(t)$ ,

These cross sections are denoted in the following as  $[y(t), p_T(t)]$ , etc.

2. triple-differential cross sections as a function of  $N_{\text{jet}}$ ,  $M(t\bar{t})$  and  $y(t\bar{t})$ . This cross section is measured separately using two ( $N_{\text{jet}} = 0$  and  $N_{\text{jet}} \geq 1$ ) and three ( $N_{\text{jet}} = 0$ ,  $N_{\text{jet}} = 1$ , and  $N_{\text{jet}} \geq 2$ ) bins of  $N_{\text{jet}}$ , for the particle level jets. These cross sections are denoted as  $[N_{\text{jet}}^{0,1+}, M(t\bar{t}), y(t\bar{t})]$  and  $[N_{\text{jet}}^{0,1,2+}, M(t\bar{t}), y(t\bar{t})]$ , respectively.

The pairs of variables for the double-differential cross sections are chosen in order to obtain representative combinations that are sensitive to different aspects of the  $t\bar{t}$  production dynamics, mostly following the previous measurement [17]. The variables for the triple-differential cross sections are chosen in order to enhance sensitivity to the PDFs,  $\alpha_s$  and  $m_t^{\text{pole}}$ . In particular, the combination of  $y(t\bar{t})$  and  $M(t\bar{t})$  variables provides sensitivity for the PDFs, as demonstrated in [17], the  $N_{\text{jet}}$  distribution for  $\alpha_s$  and  $M(t\bar{t})$  for  $m_t^{\text{pole}}$ .

On average, the total uncertainties for all measured cross sections are about 5–10%, but reach 20% and more in some regions of phase space, such as the last  $N_{\text{jet}}$  range of the  $[N_{\text{jet}}^{0,1,2+}, M(t\bar{t}), y(t\bar{t})]$ . The total uncertainties are dominated by the systematic uncertainties receiving similar contributions from the experimental and signal modelling systematic sources. The largest experimental systematic uncertainty is the JES. Both the JES and signal modelling systematics are

also affected by the statistical uncertainties in the simulated samples that are used for the evaluation of these uncertainties.

In Figs. 3–11 the measured cross sections are compared to three theoretical predictions based on MC simulations: POWHEGV2 + PYTHIA8 ('POW-PYT'), POWHEGV2 + HERWIG++ ('POW-HER'), and MG5\_aMC@NLO + PYTHIA8 ('FXFX-PYT'). For each comparison, a  $\chi^2$  is reported which is calculated taking into account the statistical and systematic data uncertainties only. The  $\chi^2$  values are calculated as follows:

$$\chi^2 = \mathbf{R}_{N-1}^T \mathbf{Cov}_{N-1}^{-1} \mathbf{R}_{N-1}, \quad (2)$$

where  $\mathbf{R}_{N-1}$  is the column vector of the residuals calculated as the difference of the measured cross sections and the corresponding predictions obtained by discarding one of the  $N$  bins, and  $\mathbf{Cov}_{N-1}$  is the  $(N-1) \times (N-1)$  submatrix obtained from the full covariance matrix by discarding the corresponding row and column. The matrix  $\mathbf{Cov}_{N-1}$  obtained in this way is invertible, while the original covariance matrix  $\mathbf{Cov}$  is singular because for normalised cross sections one degree of freedom is lost, as can be deduced from Eq. (1). The covariance matrix  $\mathbf{Cov}$  is calculated as:

$$\mathbf{Cov} = \mathbf{Cov}^{\text{unf}} + \mathbf{Cov}^{\text{syst}}, \quad (3)$$

where  $\mathbf{Cov}^{\text{unf}}$  and  $\mathbf{Cov}^{\text{syst}}$  are the covariance matrices corresponding to the statistical uncertainties from the unfolding, and the systematic uncertainties, respectively. The systematic covariance matrix  $\mathbf{Cov}^{\text{syst}}$  is calculated as:

$$\mathbf{Cov}_{ij}^{\text{syst}} = \sum_{k,l} \frac{1}{N_k} C_{j,k,l} C_{i,k,l}, \quad 1 \leq i \leq N, \quad 1 \leq j \leq N, \quad (4)$$

where  $C_{i,k,l}$  stands for the systematic uncertainty from variation  $l$  of source  $k$  in the  $i$ th bin, and  $N_k$  is the number of variations for source  $k$ . The sums run over all sources of the systematic uncertainties and all corresponding variations. Most of the systematic uncertainty sources in this analysis consist of positive and negative variations and thus have  $N_k = 2$ , whilst several model uncertainties (the model of color reconnection and the  $b$  quark fragmentation function) consist of more than two variations which is accounted for in Eq. 4. All systematic uncertainties are treated as additive, i.e. the relative uncertainties are used to scale the corresponding measured value in the construction of  $\mathbf{Cov}^{\text{syst}}$ . This treatment is consistent with the cross section normalization. The cross section measurements for different multi-differential distributions are statistically and systematically correlated. No attempt is made to quantify the correlations between bins from different multi-differential distributions. Thus, quantitative comparisons between theoretical predictions and the data can only be made for each single set of multi-differential cross sections.

In Fig. 3, the  $p_T(t)$  distribution is compared in different ranges of  $|y(t)|$  to predictions from 'POW-PYT', 'POW-HER', and 'FXFX-PYT'. The data distribution is softer than that of the predictions over the entire  $y(t)$  range. Only 'POW-HER' describes the data well, while the other two simulations predict a harder  $p_T(t)$  distribution than measured in the data over the entire  $y(t)$  range. The disagreement is strongest for 'POW-PYT'.

Figures 4 and 5 illustrate the distributions of  $|y(t)|$  and  $|y(t\bar{t})|$  in different  $M(t\bar{t})$  ranges compared to the same set of MC models. The shapes of the  $y(t)$  and  $y(t\bar{t})$  distributions are reasonably well modelled by all models, except for the largest  $M(t\bar{t})$  range, where all theoretical predictions are more central than the data for  $y(t)$  and less central for  $y(t\bar{t})$ . The  $M(t\bar{t})$  distribution is softer in the data than in the theoretical predictions. The latter trend is the strongest for

‘POW-PYT’, being consistent with the disagreement for the  $p_T(t)$  distribution (see Fig. 3). The best agreement for both  $[M(t\bar{t}), y(t)]$  and  $[M(t\bar{t}), y(t\bar{t})]$  cross sections is provided by ‘POW-HER’.

In Fig. 6, the  $\Delta\eta(t, \bar{t})$  distribution is compared in the same  $M(t\bar{t})$  ranges to the theoretical predictions. For all generators there is a discrepancy between the data and simulation for the medium and high  $M(t\bar{t})$  bins, where the predicted  $\Delta\eta(t, \bar{t})$  values are too low. The disagreement is the strongest for ‘FXFX-PYT’.

Figures 7 and 8 illustrate the comparison of the distributions of  $\Delta\phi(t, \bar{t})$  and  $p_T(t\bar{t})$  in the same  $M(t\bar{t})$  ranges to the theoretical predictions. Both these distributions are sensitive to gluon radiation. All MC models describe the data well within uncertainties, except for ‘FXFX-PYT’, which predicts a  $p_T(t\bar{t})$  distribution in the last  $M(t\bar{t})$  bin of the  $[M(t\bar{t}), p_T(t\bar{t})]$  cross sections that is too hard.

In Fig. 9, the  $p_T(t)$  distribution is compared in different  $M(t\bar{t})$  ranges to the theoretical predictions. None of the MC generators is able to describe the data, generally predicting a too hard  $p_T(t)$  distribution. The discrepancy is larger at high  $M(t\bar{t})$  values where the softer  $p_T(t)$  spectrum in the data must be kinematically correlated with the larger  $\Delta\eta(t, \bar{t})$  values (see Fig. 6), compared to the predictions. The disagreement is the strongest for ‘POW-PYT’. While the ‘POW-HER’ simulation is able to reasonably describe the  $p_T(t)$  distribution in the entire range of  $y(t\bar{t})$  (see Fig. 3), it does not provide a good description in all ranges of  $M(t\bar{t})$ , in particular predicting a too hard  $p_T(t)$  distribution at high  $M(t\bar{t})$ .

Figures 10 and 11 illustrate the triple-differential cross sections as a function of  $y(t\bar{t})$  in different  $M(t\bar{t})$  and  $N_{\text{jet}}$  ranges, measured using two or three bins of  $N_{\text{jet}}$ . For the  $[N_{\text{jet}}^{0,1+}, M(t\bar{t}), y(t\bar{t})]$  measurement, all MC models describe the data well. For the  $[N_{\text{jet}}^{0,1,2+}, M(t\bar{t}), y(t\bar{t})]$  measurement, only ‘POW-PYT’ is in satisfactory agreement with the data. In particular, ‘POW-HER’ predicts too high a cross section for  $N_{\text{jet}} > 1$ , while ‘FXFX-PYT’ provides the worst description of the  $M(t\bar{t})$  distribution for  $N_{\text{jet}} = 1$ .

All obtained  $\chi^2$  values, ignoring theoretical uncertainties, together with the corresponding numbers of degrees of freedom (dof), are listed in Table 1. The corresponding  $p$ -values are visualised in Fig. 12. From these values one can conclude that none of the central predictions of the considered MC generators is able to provide predictions that correctly describe all distributions. In particular, for  $[M(t\bar{t}), \Delta\eta(t, \bar{t})]$  and  $[M(t\bar{t}), p_T(t)]$  the  $\chi^2$  values are relatively large for all MC generators. In total, the best agreement with the data is provided by ‘POW-PYT’ and ‘POW-HER’, with POWHEGV2 + HERWIG++ better describing the measurements involving probes of the  $p_T$  distribution and ‘POW-PYT’ better describing the ones probing  $N_{\text{jet}}$  and radiation.

## 8 Extraction of $\alpha_s$ and $m_t^{\text{pole}}$ from $[N_{\text{jet}}^{0,1+}, M(t\bar{t}), y(t\bar{t})]$ cross sections using external PDFs

To extract  $\alpha_s$  and  $m_t^{\text{pole}}$ , the measured triple-differential cross sections are compared to fixed-order (NLO) predictions, which do not have variable parameters, except for factorisation and renormalisation scales, and thus allow a more rigorous assessment of theoretical uncertainties than predictions of MC event generators that complement fixed-order computations with parton showers, hadronisation, and multiple-parton interactions. Furthermore, for PDF fits using these data (see Section 9), fast computation techniques have to be used which currently are available only for fixed-order calculations.

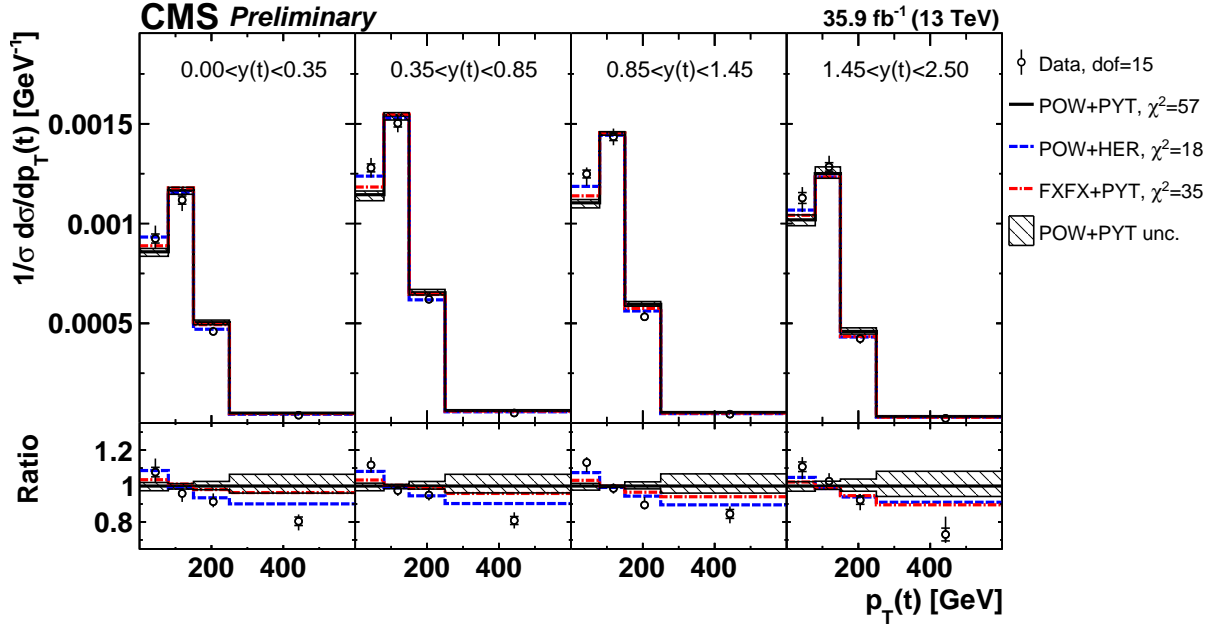


Figure 3: Comparison of the measured  $[y(t), p_T(t)]$  cross sections to the theoretical predictions calculated using POWHEGV2 + PYTHIA8 ('POW-PYT'), POWHEGV2 + HERWIG++ ('POW-HER'), and MG5\_aMC@NLO + PYTHIA8 ('FXFX-PYT') event generators. The inner vertical bars on the data points represent the statistical uncertainties and the full bars include also the systematic uncertainties added in quadrature. For each MC model, a  $\chi^2/\text{dof}$  for the comparison with the data is reported. The hatched regions correspond to the theoretical uncertainties in POWHEGV2 + PYTHIA8 (see Section 6). In the bottom panel, the ratios of the data and other simulations to the 'POW-PYT' predictions are shown.

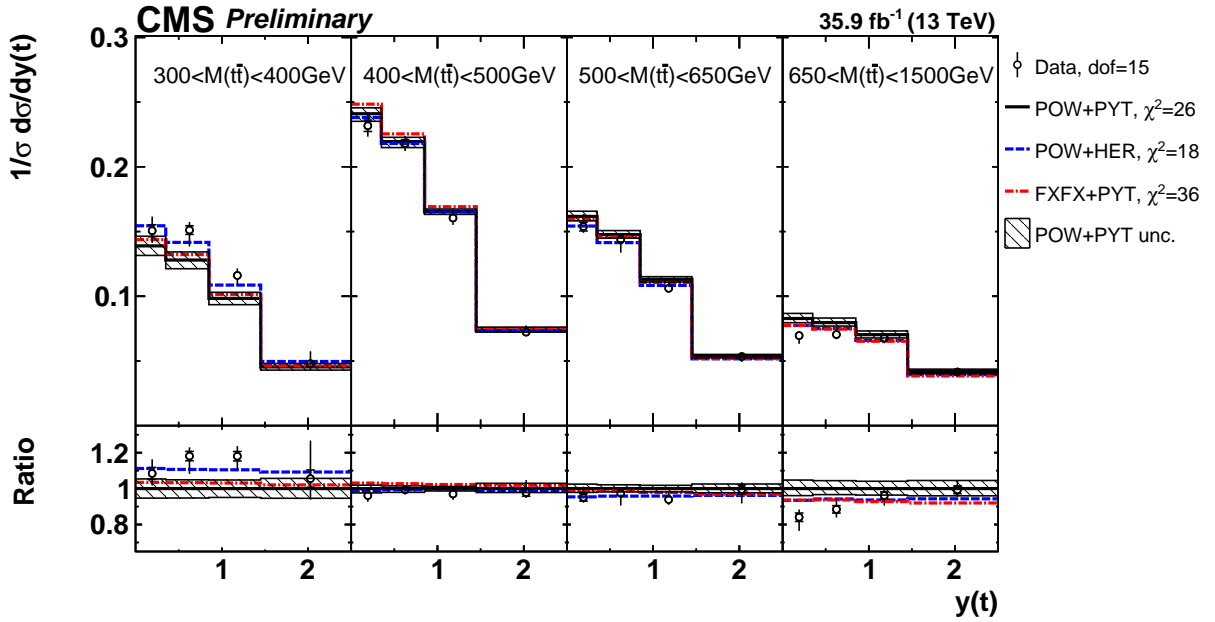


Figure 4: Comparison of the measured  $[M(t\bar{t}), y(t)]$  cross sections to the theoretical predictions calculated using MC event generators (see Fig. 3 for further details).

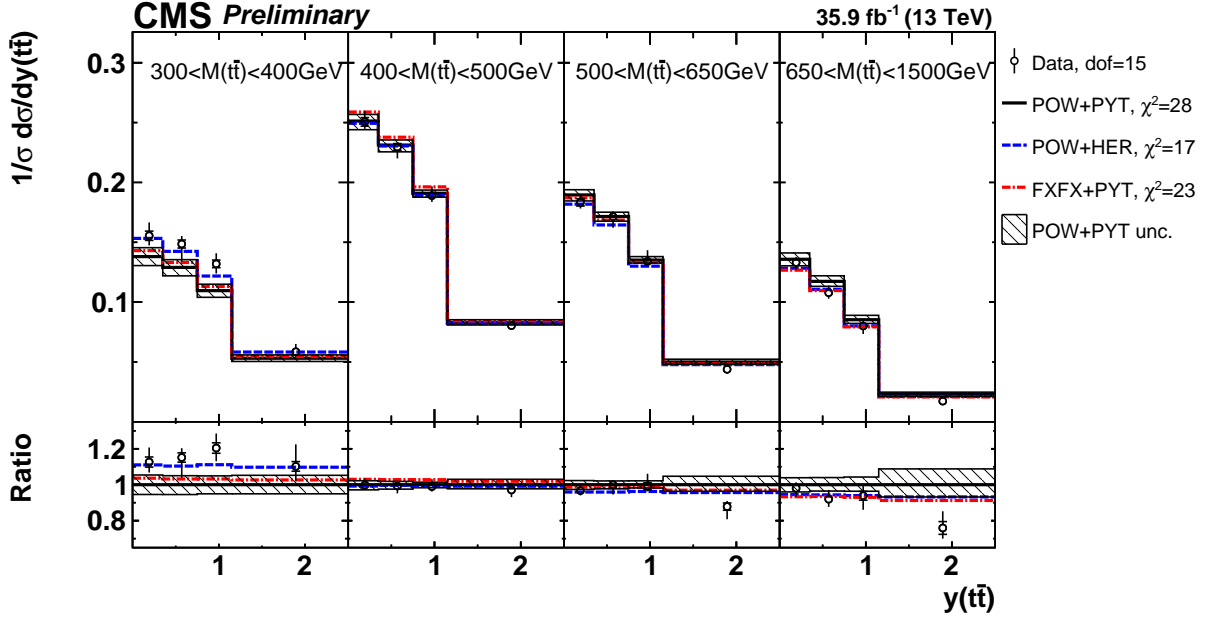


Figure 5: Comparison of the measured  $[M(t\bar{t}), y(t\bar{t})]$  cross sections to the theoretical predictions calculated using MC event generators (see Fig. 3 for further details).

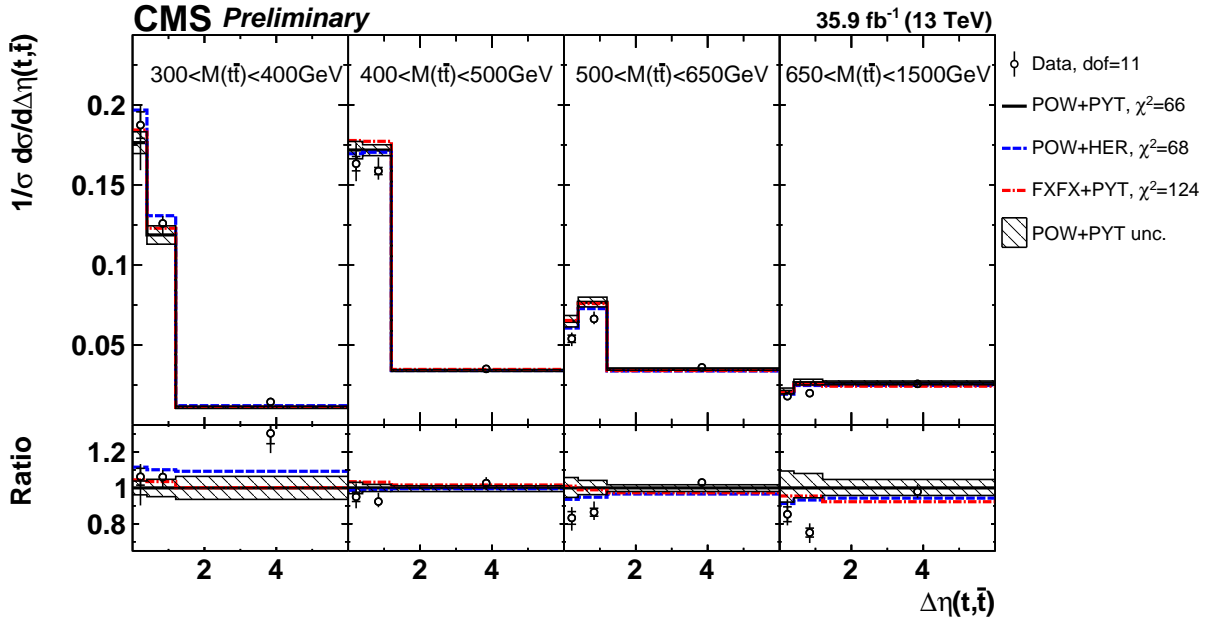


Figure 6: Comparison of the measured  $[M(t\bar{t}), \Delta\eta(t, \bar{t})]$  cross sections to the theoretical predictions calculated using MC event generators (see Fig. 3 for further details).



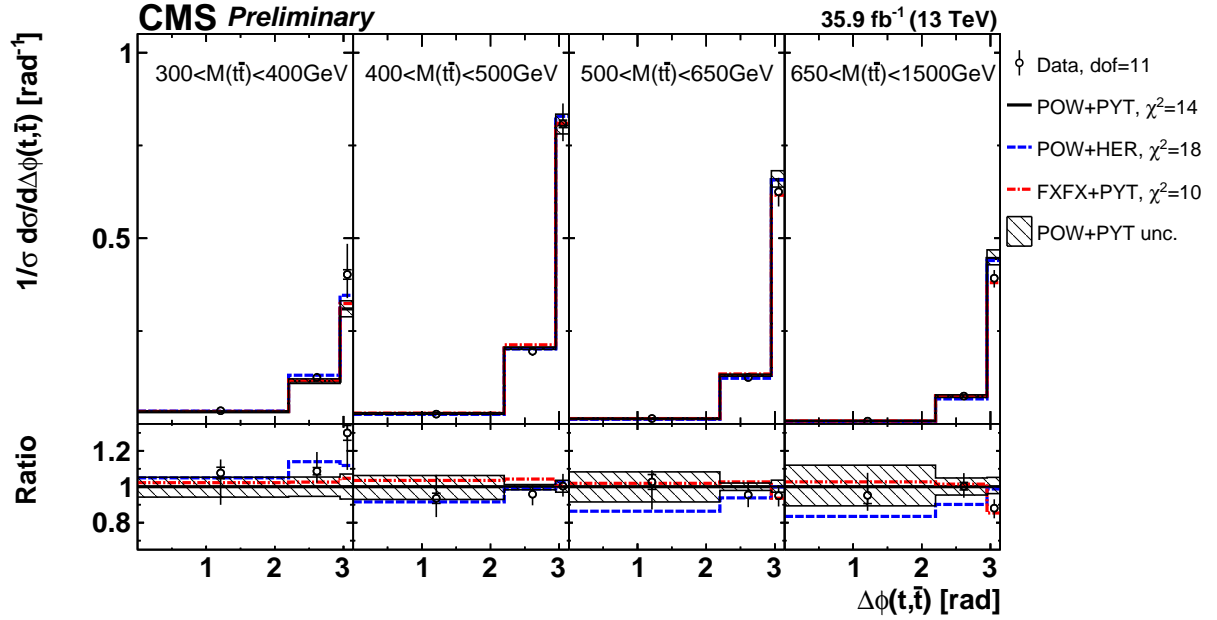


Figure 7: Comparison of the measured  $[M(t\bar{t}), \Delta\phi(t, \bar{t})]$  cross sections to the theoretical predictions calculated using MC event generators (see Fig. 3 for further details).

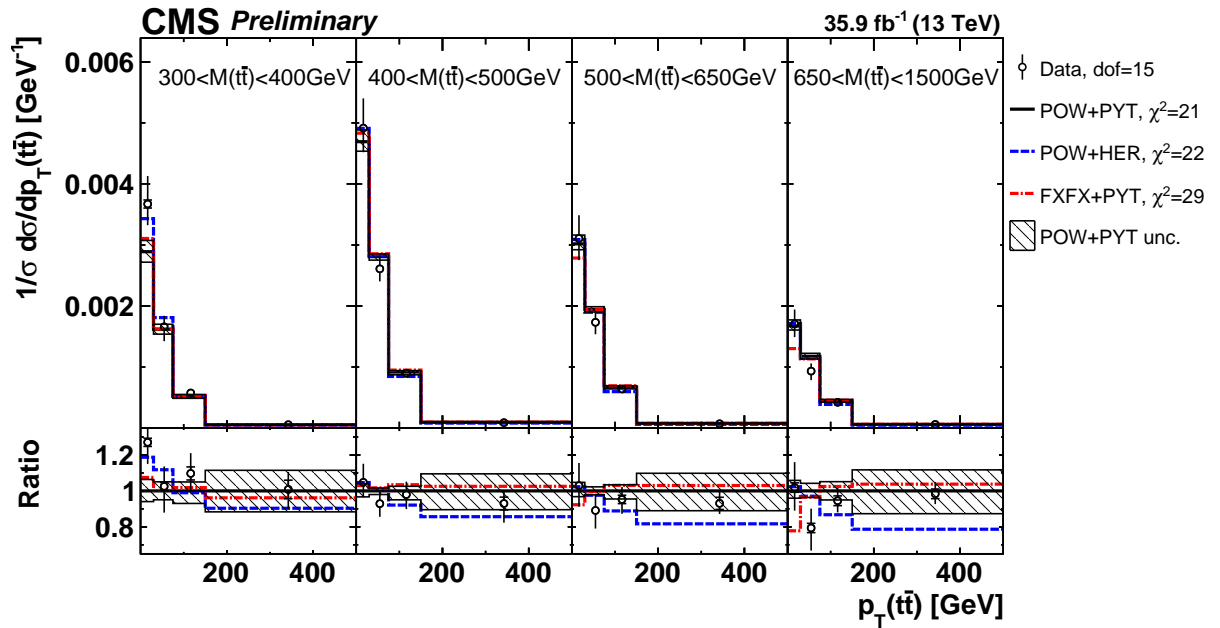


Figure 8: Comparison of the measured  $[M(t\bar{t}), p_T(t\bar{t})]$  cross sections to the theoretical predictions calculated using MC event generators (see Fig. 3 for further details).

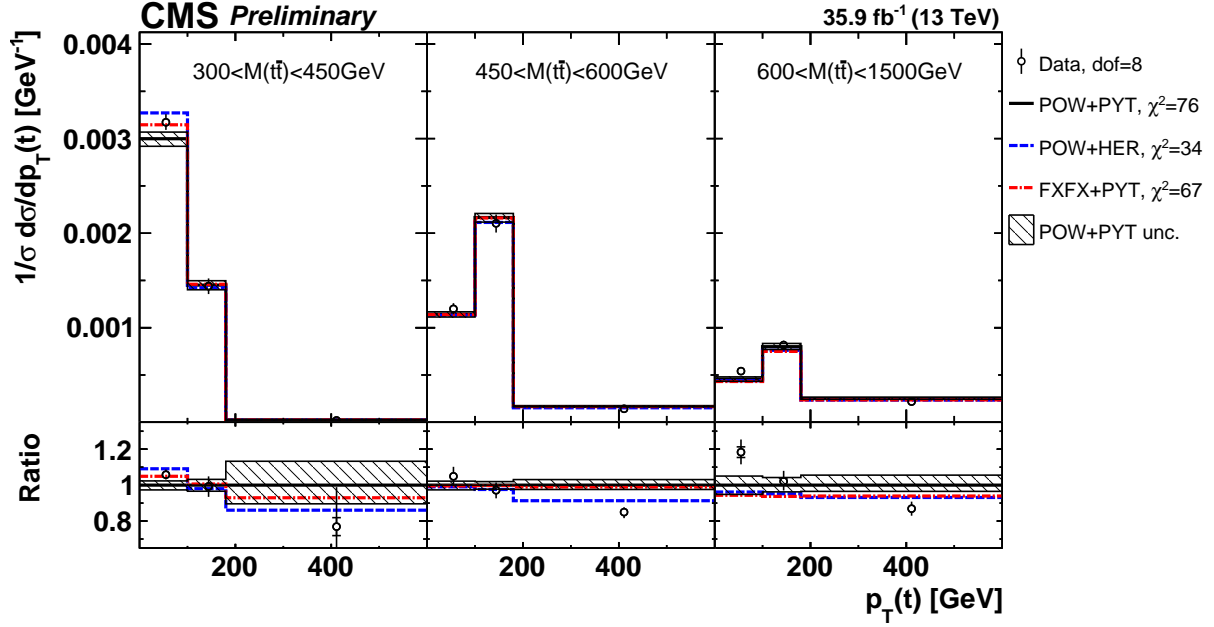


Figure 9: Comparison of the measured  $[M(t\bar{t}), p_T(t)]$  cross sections to the theoretical predictions calculated using MC event generators (see Fig. 3 for further details).

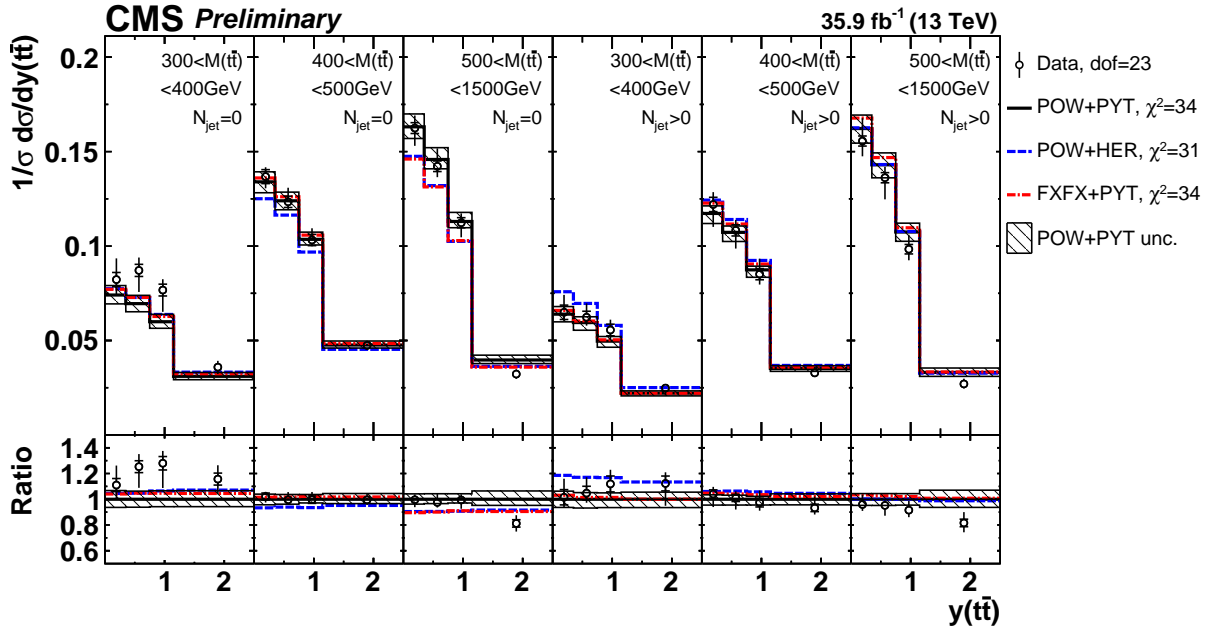


Figure 10: Comparison of the measured  $[N_{\text{jet}}^{0,1+}, M(t\bar{t}), y(t\bar{t})]$  cross sections to the theoretical predictions calculated using MC event generators (see Fig. 3 for further details).

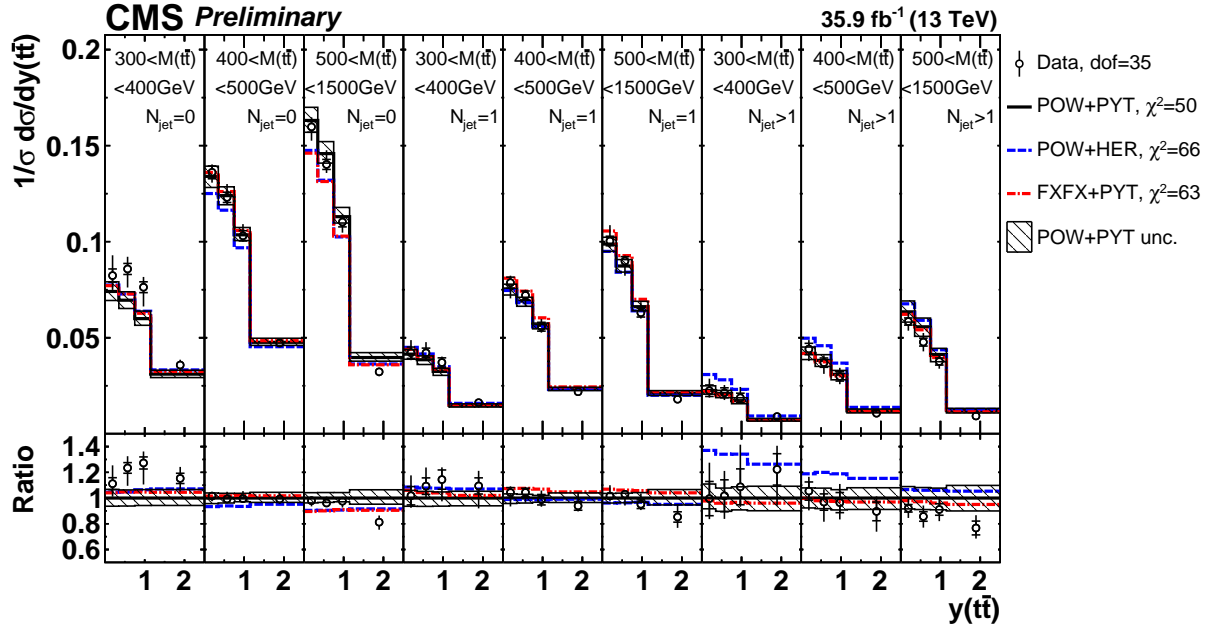


Figure 11: Comparison of the measured  $[N_{\text{jet}}^{0,1,2+}, M(t\bar{t}), y(t\bar{t})]$  cross sections to the theoretical predictions calculated using MC event generators (see Fig. 3 for further details).

Table 1: The  $\chi^2$  values (taking into account data uncertainties only) and dof of the measured cross sections with respect to the predictions of various MC generators.

Cross section variables	dof	$\chi^2$		
		'POW-PYT'	'POW-HER'	'FXFX-PYT'
$[y(t), p_T(t)]$	15	57	18	35
$[M(t\bar{t}), y(t)]$	15	26	18	36
$[M(t\bar{t}), y(t\bar{t})]$	15	28	17	23
$[M(t\bar{t}), \Delta\eta(t, \bar{t})]$	11	66	68	124
$[M(t\bar{t}), \Delta\phi(t, \bar{t})]$	15	14	18	10
$[M(t\bar{t}), p_T(t\bar{t})]$	15	21	22	29
$[M(t\bar{t}), p_T(t)]$	15	77	34	68
$[N_{\text{jet}}^{0,1+}, M(t\bar{t}), y(t\bar{t})]$	23	34	31	34
$[N_{\text{jet}}^{0,1,2+}, M(t\bar{t}), y(t\bar{t})]$	35	50	66	63

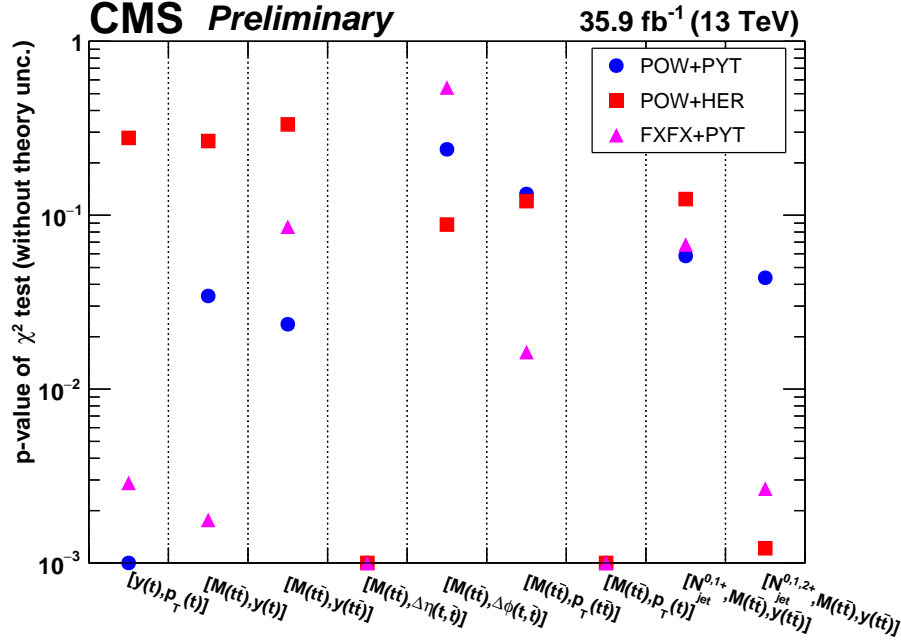


Figure 12: Assessment of compatibility of various MC predictions with the data. The plot show the  $p$ -values of  $\chi^2$ -tests between data and predictions. Only the data uncertainties are taken into account in the  $\chi^2$ -tests while uncertainties on the theory calculations are ignored. Points with  $p \leq 0.001$  are shown at  $p = 0.001$ .

Fixed-order theoretical calculations for fully differential cross sections for inclusive  $t\bar{t}$  production are publicly available at NLO  $O(\alpha_s^3)$  in the fixed-flavour number scheme [76], where  $\alpha_s$  is the strong coupling strength, and for inclusive  $t\bar{t}$  production with one [77] and two [78, 79] additional jets. These calculations are used in the present analysis. Furthermore, NLO predictions for inclusive  $t\bar{t}$  production with three additional jets exist [80], but are not used in this note because the sample of events with three additional jets is not large enough to allow us to measure multi-differential cross sections. The exact fully differential NNLO  $O(\alpha_s^4)$  calculations for inclusive  $t\bar{t}$  production have recently appeared in the literature [81, 82], but such predictions have not been published yet. NNLO calculations for inclusive  $t\bar{t}$  production with additional jets have not been performed.

The measured  $[N_{\text{jet}}^{0,1+}, M(t\bar{t}), y(t\bar{t})]$  and  $[N_{\text{jet}}^{0,1,2+}, M(t\bar{t}), y(t\bar{t})]$  cross sections are compared to NLO predictions obtained using different PDF sets,  $\alpha_s$  and  $m_t^{\text{pole}}$  values. The NLO predictions are obtained using the MG5\_aMC@NLO framework running in the fixed-order mode. The cross sections for the  $N_{\text{jet}} = 0(1)$  bin are obtained as the difference of the inclusive  $t\bar{t}$  ( $t\bar{t} + 1$  jet) and  $t\bar{t} + 1$  jet ( $t\bar{t} + 2$  jets) cross sections. The normalisation cross section is evaluated by integrating the differential cross sections over all bins, i.e. it is given by the inclusive  $t\bar{t}$  cross section. A number of the latest proton NLO PDF sets are used, namely: ABMP16 [83], CJ15 [84], CT14 [85], HERAPDF2.0 [86], JR14 [87], MMHT2014 [88], and NNPDF3.1 [89], available via the LHAPDF interface (version 6.1.5) [90]. No  $t\bar{t}$  data were used in the determination of the CJ15, CT14, HERAPDF2.0 and JR14 PDF sets; only total  $t\bar{t}$  production cross section measurements were used to determine the ABMP16 and MMHT2014 PDFs, and both total and differential (from Run-I LHC)  $t\bar{t}$  cross sections were used in the NNPDF3.1 extraction. The number of active flavours is set to  $n_f = 5$ , a top quark pole mass  $m_t^{\text{pole}} = 172.5 \text{ GeV}$  is used, and  $\alpha_s$  is set to the value used for the corresponding PDF extraction. The renormalisation and factorization

scales are chosen to be  $\mu_r = \mu_f = H'/2$ ,  $H' = \sum_i m_{T,i}$ . Here the sum is running over all final-state partons (t,  $\bar{t}$  and up to three light partons in the  $\text{t}\bar{\text{t}} + 2$  jet calculations) and  $m_T$  denotes a transverse mass defined as  $m_T = \sqrt{m^2 + p_T^2}$ . The theoretical uncertainty is estimated by varying  $\mu_r$  and  $\mu_f$  independently up and down by a factor of 2, with the additional restriction that the ratio  $\mu_r/\mu_f$  stays between 0.5 and 2 [91]. Additionally, an alternative scale choice  $\mu_r = \mu_f = H/2$ ,  $H = \sum_i m_{T,i}$ , with the sum running only over t and  $\bar{t}$  [82], is considered. The scales are varied coherently in the predictions with different  $N_{\text{jet}}$ . The final uncertainty is determined as an envelope of all scale variations on the normalised cross sections. This uncertainty is referred to hereafter as a scale uncertainty and is supposed to estimate the impact of missing higher orders. The PDF uncertainties are taken into account in the theoretical predictions for each PDF set. The PDF uncertainties of CJ15 [84] and CT14 [85], evaluated at 90% CL, are rescaled to the 68% CL for consistency with other PDF sets. The uncertainties in the normalised  $\text{t}\bar{\text{t}}$  cross sections originating from  $\alpha_s$  and  $m_t$  are estimated by varying them  $\alpha_s = 0.118 \pm 0.001$  and  $m_t^{\text{pole}} = 172.5 \pm 1$  GeV, respectively (for presentation purposes, in some figures larger variations  $\alpha_s = 0.118 \pm 0.005$  and  $m_t^{\text{pole}} = 172.5 \pm 5$  GeV are shown).

To compare the measured cross sections to the NLO QCD calculations, the latter are further corrected from parton to particle level. The NLO QCD calculations are provided for parton-level jets and stable top quarks, therefore the corrections (further referred to as non-perturbative, NP) are determined using additional POWHEGV2 + PYTHIA8 MC simulations for  $\text{t}\bar{\text{t}}$  production with and without multiparton interactions (MPI), hadronisation and top quark decays, and defined as:

$$\mathcal{C}_{\text{NP}} = \frac{\sigma_{\text{isolated from t} \rightarrow \ell, \text{b}}^{\text{particle}}}{\sigma_{\text{no MPI, no had., no t}\bar{\text{t}} \text{ decays}}^{\text{parton}}}. \quad (5)$$

Here  $\sigma_{\text{isolated from t} \rightarrow \ell, \text{b}}^{\text{particle}}$  is the cross section with MPI and hadronisation for jets built of particles excluding neutrinos and isolated from charged leptons and b quarks from the top quark decays, as defined in Section 3, and  $\sigma_{\text{no MPI, no had., no t}\bar{\text{t}} \text{ decays}}^{\text{parton}}$  is the cross section without MPI and hadronisation for jets built of partons excluding t and  $\bar{t}$ . The  $\mathcal{C}_{\text{NP}}$  factors are used to correct the NLO predictions to particle level. The NP corrections are determined in bins of the triple-differential cross sections as a function of  $N_{\text{jet}}$ ,  $M(\text{t}\bar{\text{t}})$  and  $y(\text{t}\bar{\text{t}})$ , even though they depend primarily on  $N_{\text{jet}}$  and have only weak dependence on the  $\text{t}\bar{\text{t}}$  kinematics. For the cross sections with up to two extra jets measured in this analysis, the estimated NP corrections are small, within 5%. The dependence of the NP corrections on MC modelling was studied using MC samples with varied hadronisation model, underlying event tune, matrix element and parton shower scales as detailed in Section 6. All resulting variations of  $\mathcal{C}_{\text{NP}}$  were found to be  $\lesssim 1\%$ , therefore no uncertainties on the determined NP corrections are assigned. To compare to the measured cross sections, the normalised multi-differential cross sections of the theory predictions are obtained by dividing the cross sections in specific bins by the total cross section summed over all bins.

The theoretical uncertainties for the  $[N_{\text{jet}}^{0,1+}, M(\text{t}\bar{\text{t}}), y(\text{t}\bar{\text{t}})]$  and  $[N_{\text{jet}}^{0,1,2+}, M(\text{t}\bar{\text{t}}), y(\text{t}\bar{\text{t}})]$  cross sections are shown in Fig. 13. The CT14 PDF set with  $\alpha_s(M_Z) = 0.118$ ,  $m_t^{\text{pole}} = 172.5$  GeV is used as the nominal calculation. The contributions arising from the PDF,  $\alpha_s \pm 0.005$  and  $m_t^{\text{pole}} \pm 1$  GeV uncertainties are shown separately. The total theoretical uncertainties are obtained by adding the PDF,  $\alpha_s$  and  $m_t^{\text{pole}}$  and scale uncertainties in quadrature. On average, the total theoretical uncertainties are 5–10%. They receive similar contribution from PDF,  $\alpha_s$ ,  $m_t^{\text{pole}}$  and scale variations. This shows that the measured  $[N_{\text{jet}}^{0,1+}, M(\text{t}\bar{\text{t}}), y(\text{t}\bar{\text{t}})]$  cross sections can be used for reliable and precise extraction of the PDFs and QCD parameters. In this analysis the PDFs,  $\alpha_s$

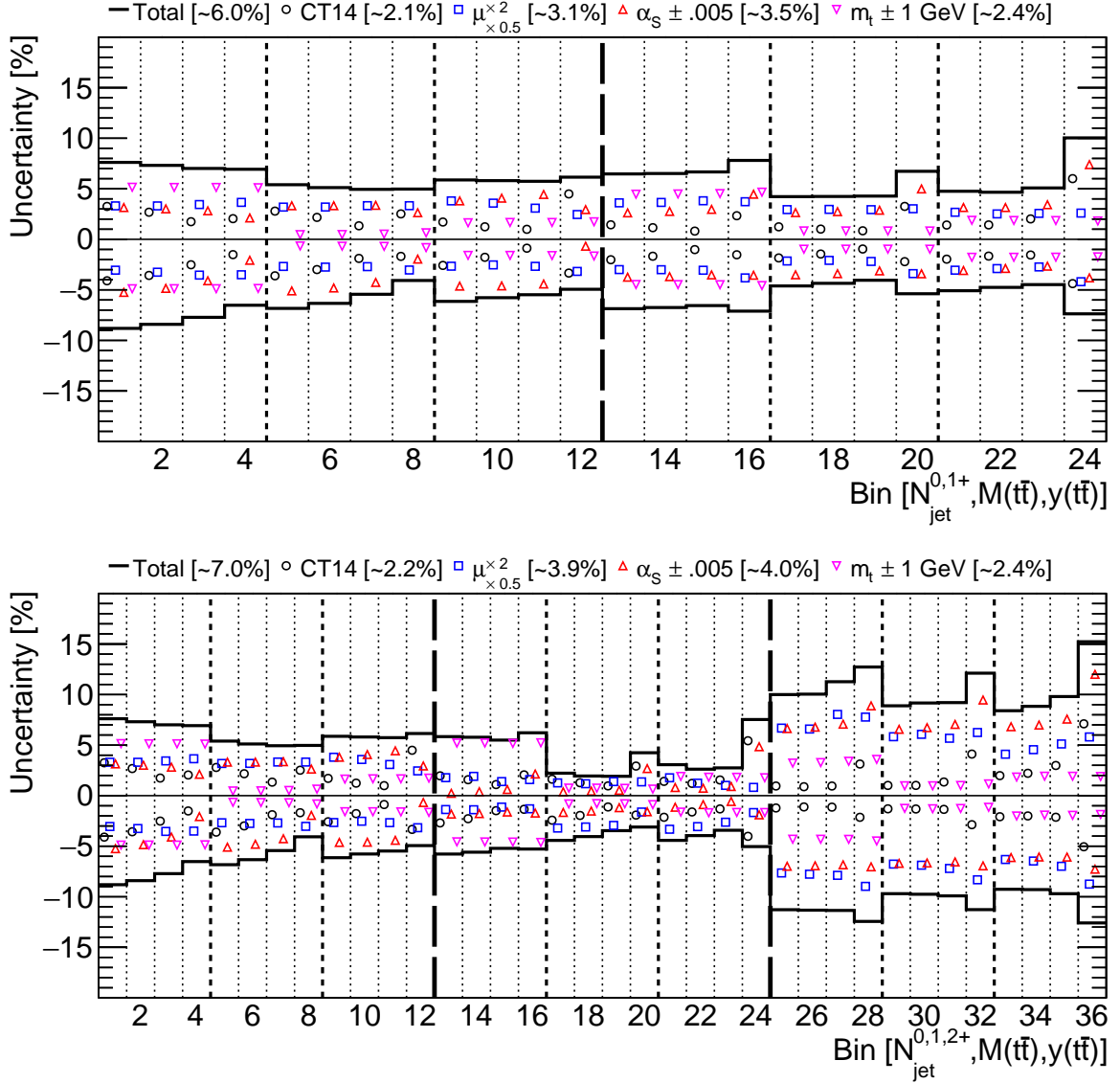


Figure 13: The theoretical uncertainties for  $[N_{\text{jet}}^{0,1+}, M(t\bar{t}), y(t\bar{t})]$  (top) and  $[N_{\text{jet}}^{0,1,2+}, M(t\bar{t}), y(t\bar{t})]$  (bottom) cross sections, arising from PDF,  $\alpha_s$  and  $m_t^{\text{pole}}$  variations, as well as the total theoretical uncertainties, with their bin averaged values shown in brackets. The bins are the same as in Figs. 10 and 11.

and  $m_t^{\text{pole}}$  are extracted from the  $[N_{\text{jet}}^{0,1+}, M(t\bar{t}), y(t\bar{t})]$  cross sections. These results are considered to be the nominal ones and are checked by repeating the analysis using the  $[N_{\text{jet}}^{0,1,2+}, M(t\bar{t}), y(t\bar{t})]$  cross sections.

In Figs. 14–16 the  $[N_{\text{jet}}^{0,1+}, M(t\bar{t}), y(t\bar{t})]$  cross sections are compared to the predictions obtained using different PDFs,  $\alpha_s$  and  $m_t^{\text{pole}}$  values. For each comparison, a  $\chi^2$  is calculated which takes into account data only or data and PDF uncertainties, i.e. Eq. (3) becomes  $\mathbf{Cov} = \mathbf{Cov}^{\text{unf}} + \mathbf{Cov}^{\text{syst}} + \mathbf{Cov}^{\text{PDF}}$ , where  $\mathbf{Cov}^{\text{PDF}}$  is a covariance matrix that accounts for the PDF uncertainties. Theoretical uncertainties from scale,  $\alpha_s$  and  $m_t^{\text{pole}}$  variations are not included in this  $\chi^2$  calculation. Sizable differences of the  $\chi^2$  values are observed for the predictions obtained with using different PDFs. Among the PDF sets considered, the best description of the data is pro-

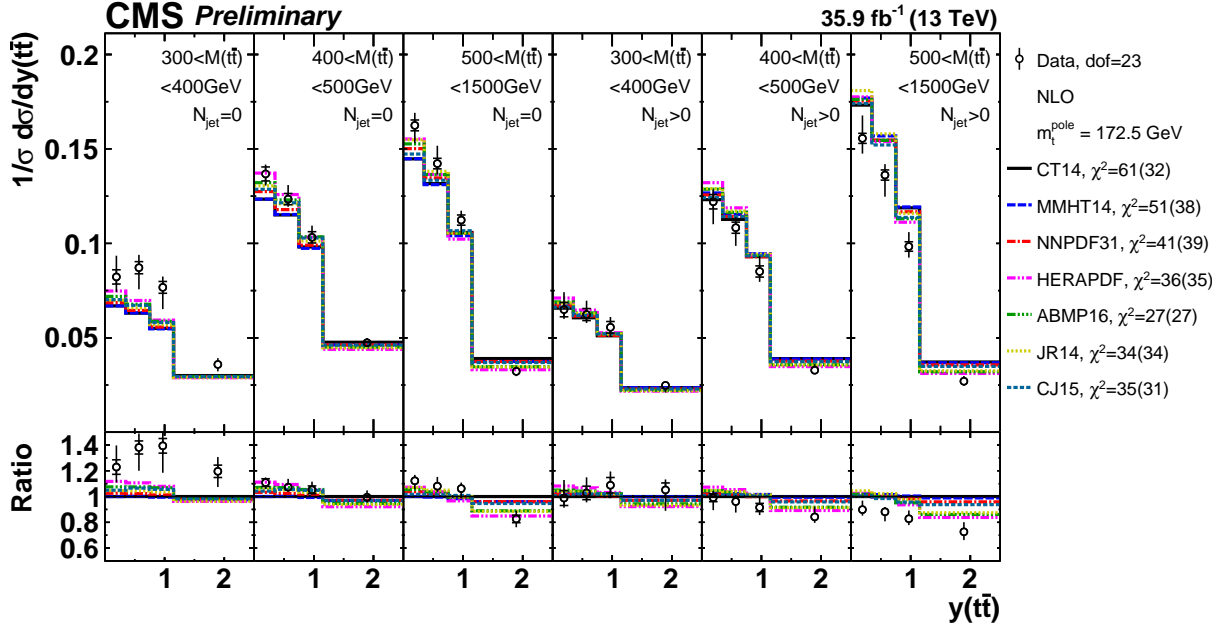


Figure 14: Comparison of the measured  $[N_{\text{jet}}^{0,1+}, M(t\bar{t}), y(t\bar{t})]$  cross sections to NLO predictions obtained using different PDF sets. For each theoretical prediction, a  $\chi^2/\text{dof}$  for the comparison to the data is reported, while additional  $\chi^2$  values that include PDF uncertainties are shown in parentheses.

vided by the ABMP16 PDFs. This comparison also shows that the data prefer lower  $\alpha_s$  and  $m_t^{\text{pole}}$  value than in the nominal calculation using CT14.

The values of  $\alpha_s$  and  $m_t^{\text{pole}}$  are extracted by calculating  $\chi^2$  between the data and NLO predictions as a function of the input  $\alpha_s$  or  $m_t^{\text{pole}}$  value and approximating the dependence with a parabola. The minimum of the parabola is taken as the extracted  $\alpha_s$  or  $m_t^{\text{pole}}$  value, while its uncertainty is estimated from the  $\Delta\chi^2 = 1$  variation. This extraction is performed separately using different PDF sets, as well as different scale values. Among the available PDF sets, only CT14, HERAPDF2.0 and ABMP16 provide PDF sets for enough different  $\alpha_s$  values and are suitable for  $\alpha_s$  extraction. Furthermore, to assess the correlation between  $\alpha_s$  and  $m_t^{\text{pole}}$ , the extraction of  $\alpha_s$  ( $m_t^{\text{pole}}$ ) is performed for different  $m_t^{\text{pole}}$  ( $\alpha_s$ ) values.

The  $\alpha_s$  and  $m_t^{\text{pole}}$  scans for different PDF sets are shown in Fig. 17. The extracted  $\alpha_s$  and  $m_t^{\text{pole}}$  values are reported on the plots. Furthermore, the  $\alpha_s$  ( $m_t^{\text{pole}}$ ) scans were performed using altered scale and  $m_t^{\text{pole}}$  ( $\alpha_s$ ) settings and different PDF sets. For all input PDF sets, the impact of the scale variations is moderate and a weak positive correlation ( $\sim 30\%$ ) between  $\alpha_s$  and  $m_t^{\text{pole}}$  is observed (the plots are available in Appendix A).

The extracted  $\alpha_s$  and  $m_t^{\text{pole}}$  values are compared in Fig. 18. The contributions to the total uncertainty arising from the data and from the theory prediction due to PDF, scale and  $m_t^{\text{pole}}$  or  $\alpha_s$  uncertainties are shown separately. For the extraction of  $\alpha_s$ , the uncertainties from the data and from PDF, scale and  $m_t^{\text{pole}}$  are comparable in magnitude. The size of the PDF uncertainties vary significantly for different PDF sets, and the extracted  $\alpha_s$  values depend on the input PDFs because of a strong correlation between  $\alpha_s$  and the gluon distribution. This illustrates that precise and reliable  $\alpha_s$  extraction from the observed data can be obtained only in a simultaneous PDF

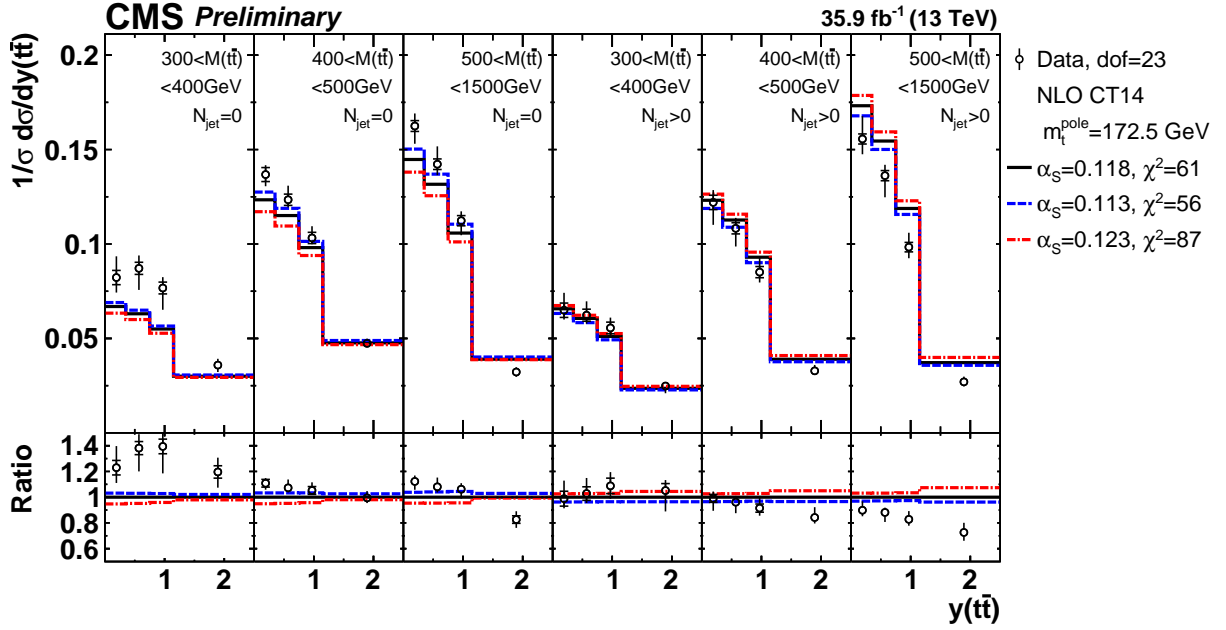


Figure 15: Comparison of the measured  $[N_{\text{jet}}^{0,1+}, M(t\bar{t}), y(t\bar{t})]$  cross sections to NLO predictions obtained using different  $\alpha_s$  values. For each theoretical prediction, a  $\chi^2/\text{dof}$  for the comparison to the data is reported.

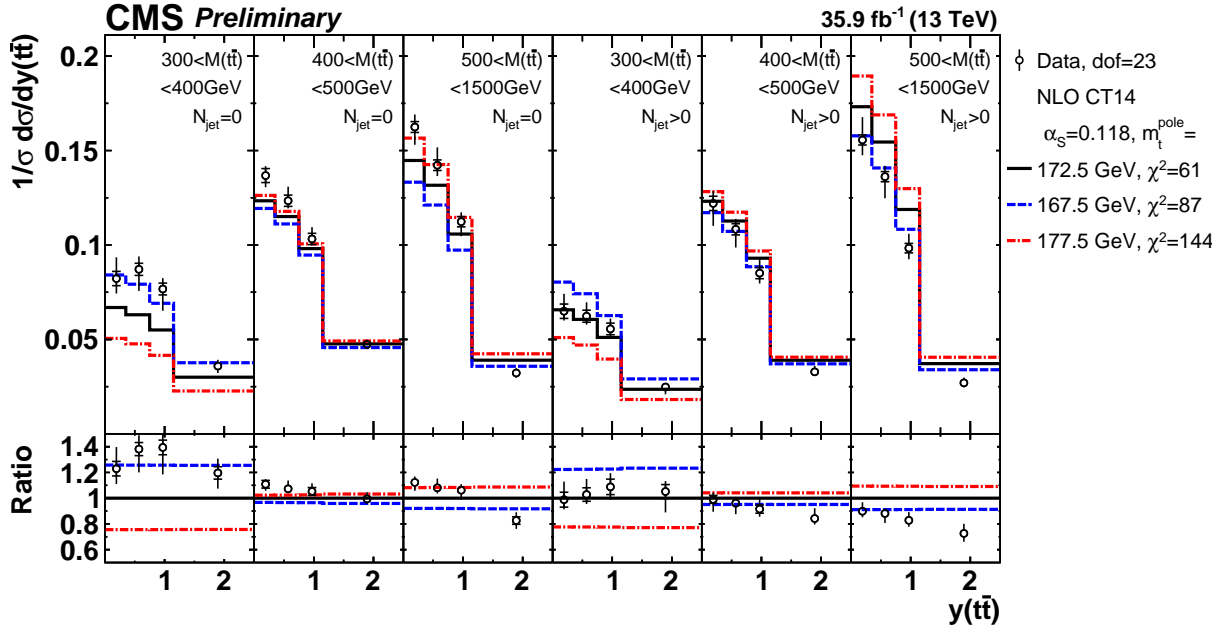


Figure 16: Comparison of the measured  $[N_{\text{jet}}^{0,1+}, M(t\bar{t}), y(t\bar{t})]$  cross sections to NLO predictions obtained using different  $m_t^{\text{pole}}$  (bottom) values. For each theoretical prediction, a  $\chi^2/\text{dof}$  for the comparison to the data is reported.



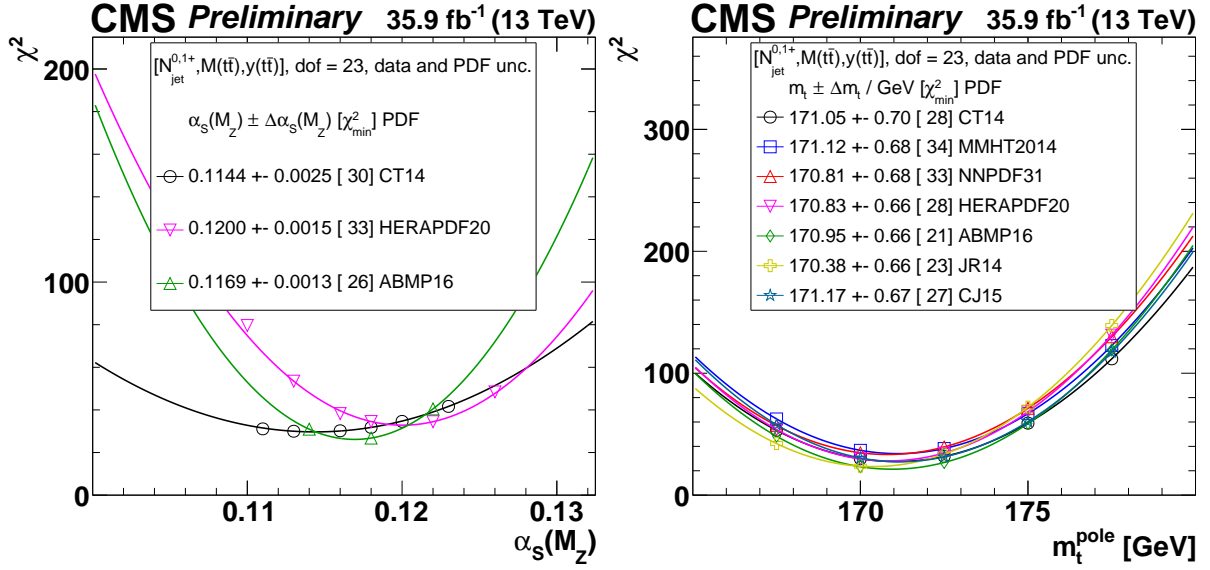


Figure 17: The  $\alpha_s$  (left) and  $m_t^{\text{pole}}$  (right) extraction at NLO from the measured  $[N_{\text{jet}}^{0,1+}, M(t\bar{t}), y(t\bar{t})]$  cross sections using different PDF sets. The extracted  $\alpha_s$  and  $m_t^{\text{pole}}$  values are reported for each PDF set, and the estimated minimum  $\chi^2$  value is shown in brackets. See the main text for further details.

and  $\alpha_s$  fit. For the  $m_t^{\text{pole}}$  extraction, the total uncertainty is dominated by the data uncertainties.

Near the mass threshold, relevant for the  $m_t^{\text{pole}}$  extraction, the perturbation series should be improved with all order soft gluon resummation which, however, is not available in the tools used to obtain theoretical predictions in this work. In Ref. [92] these effects are found to be relevant only very close to the threshold (within a few GeV) and give a correction of about +1% to the total  $t\bar{t}$  cross section. Attributing a 1% correction to the first  $M(t\bar{t})$  bin and assuming it is independent of  $y(t\bar{t})$  and  $N_{\text{jet}}$  results in a shift of +0.7 GeV for the extracted value of  $m_t^{\text{pole}}$  in this analysis, which is comparable to the total uncertainty. Furthermore, the impact of the parton shower was discussed in Ref. [4], where the predictions for inclusive  $t\bar{t} + 1$  jet production obtained at NLO and using POWHEG NLO calculations matched with the PYTHIA8 parton shower have been compared (see Fig. 1 in Ref. [4]) and agreement between different approaches was found to be within 0.5 GeV for the extracted  $m_t^{\text{pole}}$ . Including resummation effects in the theoretical calculations is needed for an accurate  $m_t^{\text{pole}}$  extraction from differential  $t\bar{t}$  cross sections in the future. Furthermore, EW corrections can be significant in some regions of phase space [93, 94].

The  $\alpha_s$  and  $m_t^{\text{pole}}$  extraction is validated by repeating the procedure:

1. **Using single-differential  $N_{\text{jet}}$ ,  $M(t\bar{t})$ ,  $y(t\bar{t})$  cross sections.** The plots are available in Appendix A. The largest sensitivity to  $\alpha_s$  is observed when using the  $y(t\bar{t})$  cross sections, though it is strongly PDF dependent. The  $N_{\text{jet}}$  distribution provides a smaller  $\alpha_s$  sensitivity, but with little dependence on the PDFs. For  $m_t^{\text{pole}}$ , the largest sensitivity is observed when using the  $M(t\bar{t})$  cross sections. In fact, almost no sensitivity to  $m_t^{\text{pole}}$  is present in  $y(t\bar{t})$  or  $N_{\text{jet}}$  single-differential cross sections. All determinations using the single-differential cross sections yielded  $\alpha_s$  and  $m_t^{\text{pole}}$  values that are consistent with the nominal determination,

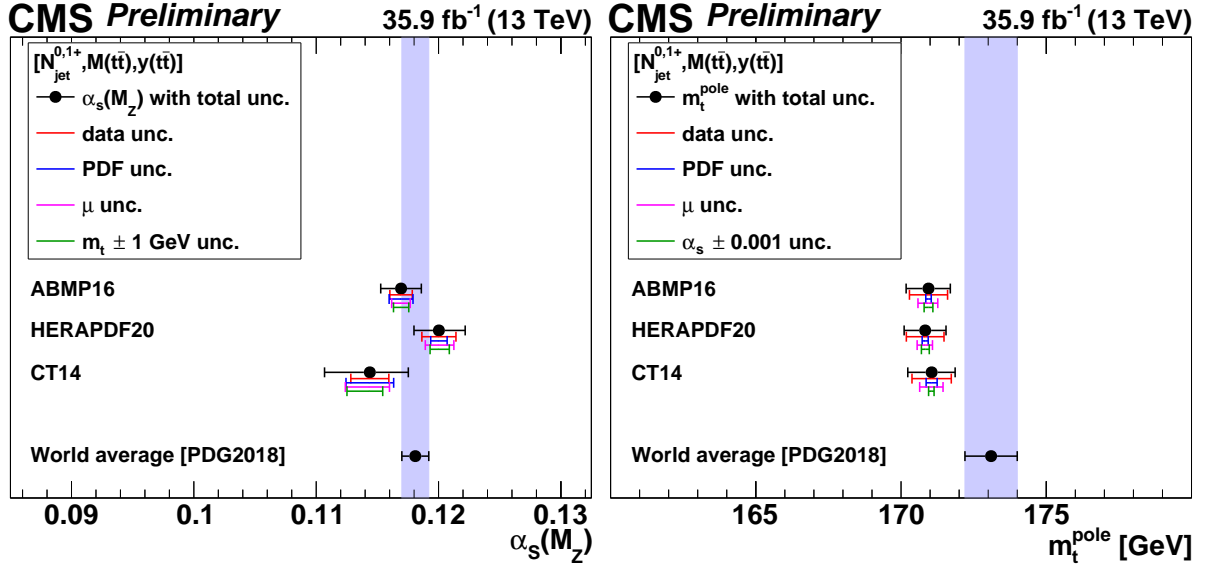


Figure 18: The  $\alpha_s$  (left) and  $m_t^{\text{pole}}$  (right) values extracted at NLO using different PDFs. The contributions to the total uncertainty arising from the data, PDF, scale and  $\alpha_s$  uncertainties are shown separately. The world average values  $\alpha_s = 0.1181 \pm 0.0011$  and  $m_t^{\text{pole}} = 173.1 \pm 0.9$  GeV from Ref. [65] are shown for reference.

2. **Using triple-differential  $[N_{\text{jet}}^{0,1,2+}, M(\text{t}\bar{\text{t}}), y(\text{t}\bar{\text{t}})]$  cross sections.** The distributions are available in Appendix A. The extracted  $\alpha_s$  and  $m_t^{\text{pole}}$  values are consistent with the nominal ones obtained using two  $N_{\text{jet}}$  bins and have similar precision with a slightly different uncertainty decomposition: smaller data uncertainties but larger scale uncertainties are present when using three  $N_{\text{jet}}$  bins. The different uncertainties are expected since more  $N_{\text{jet}}$  bins provide more sensitivity to  $\alpha_s$ , while the NLO theoretical prediction for the last  $N_{\text{jet}}$  bins (two or more extra jets) have larger scale uncertainties compared to the other bins (see Fig. 13). This shows that NLO QCD predictions are able to describe  $\text{t}\bar{\text{t}}$  data with up to two hard extra jets, however higher-order calculations are desirable to match the experimental precision in order to achieve a most accurate  $\alpha_s$  and  $m_t^{\text{pole}}$  determination.
3. **Using triple-differential  $[p_T(\text{t}\bar{\text{t}}), M(\text{t}\bar{\text{t}}), y(\text{t}\bar{\text{t}})]$  cross sections with two  $p_T(\text{t}\bar{\text{t}})$  bins.** The NLO calculations for inclusive  $\text{t}\bar{\text{t}}$  and  $\text{t}\bar{\text{t}} + 1$  jet production with an appropriate jet  $p_T$  threshold are used to describe the distribution in the two  $p_T(\text{t}\bar{\text{t}})$  bins (see Appendix A.1 for further details). The extracted  $\alpha_s$  and  $m_t^{\text{pole}}$  values (the plots are available in Appendix A.1) are consistent with the nominal ones but have slightly larger experimental, PDF and scale uncertainties compared to the nominal results using the  $[N_{\text{jet}}^{0,1+}, M(\text{t}\bar{\text{t}}), y(\text{t}\bar{\text{t}})]$  cross sections. Nevertheless, these results are an important cross check, because the  $[p_T(\text{t}\bar{\text{t}}), M(\text{t}\bar{\text{t}}), y(\text{t}\bar{\text{t}})]$  cross sections are provided at parton level and do not require non-perturbative corrections, which have to be applied for distributions involving  $N_{\text{jet}}$ .
4. **Using unnormalised cross sections.** Consistent  $\alpha_s$  and  $m_t^{\text{pole}}$  values are obtained, but with substantially larger experimental and scale uncertainties due to the increased scale dependence of the NLO predictions for the unnormalised cross sections and uncanceled normalisation uncertainties of the measured cross sections.

## 9 Simultaneous PDF, $\alpha_s$ and $m_t^{\text{pole}}$ fit

The triple-differential normalised  $[N_{\text{jet}}^{0,1+}, M(\text{t}\bar{\text{t}}), y(\text{t}\bar{\text{t}})]$  cross sections are used in a simultaneous PDF,  $\alpha_s$  and  $m_t^{\text{pole}}$  fit at NLO (also referred to as a QCD analysis, or PDF fit), together with the combined HERA inclusive deep inelastic scattering (DIS) data [86]. The xFITTER program (version 2.0.0) [95], an open-source QCD fit framework for PDF determination, is used. The precise HERA DIS data, obtained from the combination of individual H1 and ZEUS results, are directly sensitive to the valence and sea quark distributions and probe the gluon distribution through scaling violations. Therefore, these data form the core of all PDF fits. The measured  $\text{t}\bar{\text{t}}$  cross sections are included in the fit to constrain  $\alpha_s$ ,  $m_t^{\text{pole}}$  and the gluon distribution at high values of  $x$ , where  $x$  is the fraction of the proton momentum carried by a parton. The typical probed  $x$  values can be estimated using the LO kinematic relation  $x = (M(\text{t}\bar{\text{t}})/\sqrt{s}) \exp[\pm y(\text{t}\bar{\text{t}})]$ . The present measurement is expected to be mostly sensitive to  $x$  values in the region  $0.01 \lesssim x \lesssim 0.1$ , as estimated using the highest or lowest  $|y(\text{t}\bar{\text{t}})|$  or  $M(\text{t}\bar{\text{t}})$  bins and taking the low or high bin edge where the cross section is largest.

### 9.1 Details of the QCD analysis

The scale evolution of partons is calculated through DGLAP equations [96–102] at NLO, as implemented in the QCDNUM program [103] (version 17.01.14). The Thorne–Roberts [104–106] variable-flavour number scheme at NLO is used for the treatment of the heavy-quark contributions. The number of flavours is set to 5, with c and b quark mass parameters  $M_c = 1.47 \text{ GeV}$  and  $M_b = 4.5 \text{ GeV}$  [86]. For the DIS data  $\mu_r$  and  $\mu_f$  are set to  $Q$ , which denotes the four-momentum transfer. The  $Q^2$  range of the HERA data is restricted to  $Q^2 > Q_{\text{min}}^2 = 3.5 \text{ GeV}^2$  [86]. The theoretical predictions for the  $\text{t}\bar{\text{t}}$  cross sections are calculated as described in Section 8 and are included in the fit using the MG5\_aMC@NLO (version 2.6.0) [34] framework, interfaced with the AMCFast (version 1.3.0) [107] and APPLGRID (version 1.4.70) [108] programs. The strong coupling strength  $\alpha_s$  and pole top quark mass  $m_t^{\text{pole}}$  are left free in the fit.<sup>1</sup>

The procedure for the determination of the PDFs follows the approach of HERAPDF2.0 [86]. The parametrised PDFs are the gluon distribution  $xg(x)$ , the valence quark distributions  $xu_v(x)$  and  $xd_v(x)$ , and the u- and d-type antiquark distributions  $x\bar{U}(x)$  and  $x\bar{D}(x)$ . At the initial QCD evolution scale  $\mu_{f0}^2 = 1.9 \text{ GeV}^2$ , the PDFs are parametrised as:

$$\begin{aligned} xg(x) &= A_g x^{B_g} (1-x)^{C_g} (1 + E_g x^2) - A'_g x^{B'_g} (1-x)^{C'_g}, \\ xu_v(x) &= A_{u_v} x^{B_{u_v}} (1-x)^{C_{u_v}} (1 + D_{u_v} x), \\ xd_v(x) &= A_{d_v} x^{B_{d_v}} (1-x)^{C_{d_v}}, \\ x\bar{U}(x) &= A_{\bar{U}} x^{B_{\bar{U}}} (1-x)^{C_{\bar{U}}} (1 + D_{\bar{U}} x), \\ x\bar{D}(x) &= A_{\bar{D}} x^{B_{\bar{D}}} (1-x)^{C_{\bar{D}}}, \end{aligned} \tag{6}$$

assuming the relations  $x\bar{U}(x) = x\bar{u}(x)$  and  $x\bar{D}(x) = x\bar{d}(x) + x\bar{s}(x)$ . Here,  $x\bar{u}(x)$ ,  $x\bar{d}(x)$ , and  $x\bar{s}(x)$  are the up, down, and strange antiquark distributions, respectively. The sea quark distribution is defined as  $x\Sigma(x) = x\bar{u}(x) + x\bar{d}(x) + x\bar{s}(x)$ . The normalization parameters  $A_{u_v}$ ,  $A_{d_v}$ , and  $A_g$  are determined by the QCD sum rules. The  $B$  and  $B'$  parameters determine the PDFs at small  $x$ , and the  $C$  parameters describe the shape of the distributions as  $x \rightarrow 1$ . The parameter

<sup>1</sup>Technically, ApplGrid tables have been produced for fixed values of  $m_t^{\text{pole}}$ , while the theoretical predictions as a function of  $m_t^{\text{pole}}$  were obtained by linear interpolation between two predictions using different  $m_t^{\text{pole}}$  values. The results do not depend significantly on which particular  $m_t^{\text{pole}}$  values are used for linear interpolation.

$C'_g$  is fixed to 25 [109]. Additional constraints  $B_{\bar{u}} = B_{\bar{d}}$  and  $A_{\bar{u}} = A_{\bar{d}}(1 - f_s)$  are imposed to ensure the same normalization for the  $x\bar{u}$  and  $x\bar{d}$  distributions as  $x \rightarrow 0$ . The strangeness fraction  $f_s = x\bar{s}/(x\bar{d} + x\bar{s})$  is fixed to  $f_s = 0.4$  as in the HERAPDF2.0 analysis [86]. This value is consistent with the determination of the strangeness fraction when using the CMS measurements of  $W + c$  production [110].

The parameters in Eq. (6) are selected by first fitting with all  $D$  and  $E$  parameters set to zero, and then including them independently one at a time in the fit. The improvement in the  $\chi^2$  of the fit is monitored and the procedure is stopped when no further improvement is observed. This leads to a 15-parameter fit. The  $\chi^2$  definition used for the HERA DIS data follows that of Eq. (32) in Ref. [86]. It includes an additional logarithmic term that is relevant when the estimated statistical and uncorrelated systematic uncertainties in the data are rescaled during the fit [111]. For the  $t\bar{t}$  data presented here, a  $\chi^2$  definition without such a logarithmic term is employed. The treatment of the experimental uncertainties in the  $t\bar{t}$  double-differential cross section measurements follows the prescription given in Section 7. The correlated systematic uncertainties are treated through nuisance parameters. For each nuisance parameter a penalty term is added to the  $\chi^2$ , representing the prior knowledge of the parameter. The treatment of the experimental uncertainties for the HERA DIS data follows the prescription given in Ref. [86].

The uncertainties are estimated according to the general approach of HERAPDF2.0 [86] in which the fit, model, and parametrisation uncertainties are taken into account. Fit uncertainties are determined using the tolerance criterion of  $\Delta\chi^2 = 1$ . Model uncertainties arise from the variations in the values assumed for the  $c$  quark mass parameter of  $1.41 \leq M_c \leq 1.53$  GeV, the strangeness fraction  $0.3 \leq f_s \leq 0.5$ , and the value of  $Q_{\min}^2$  imposed on the HERA data. The latter is varied within  $2.5 \leq Q_{\min}^2 \leq 5.0$  GeV<sup>2</sup>, following Ref. [86]. The parametrisation uncertainty is estimated by varying the functional form in Eq. (6) of all parton distributions, with parameters  $D$  and  $E$  added or removed one at a time. Additional parametrisation uncertainties are considered by using two other functional forms in Eq. (6): with  $A'_g = 0$  and  $E_g = 0$ , since the  $\chi^2$  in these variants of the fit are only a few units worse than that with the nominal parametrisation. Furthermore,  $\mu_{f_0}^2$  is changed from  $1.9$  GeV<sup>2</sup> to  $1.6$  GeV<sup>2</sup> and  $2.2$  GeV<sup>2</sup>. The parametrisation uncertainty is constructed as an envelope, built from the maximal differences between the PDFs or QCD parameters resulting from the central fit and all parametrisation variations. For the PDFs, this uncertainty is valid in the  $x$  range covered by the PDF fit to the data. The total uncertainty is obtained by adding the fit, model, and parametrisation uncertainties in quadrature. For  $\alpha_s$  and  $m_t^{\text{pole}}$  extraction, the scale uncertainties of the theoretical predictions for  $t\bar{t}$  production are also considered. In the following, the quoted uncertainties correspond to 68% CL.

A cross check is performed using the Monte Carlo method [112, 113]. It is based on analysing a large number of pseudo-datasets called replicas. For this cross check, 1000 replicas are created by taking the pooled data and fluctuating the values of the cross sections randomly within their statistical and systematic uncertainties taking correlations into account. All uncertainties are assumed to follow Gaussian distributions. The central values for the fitted parameters and their uncertainties are estimated using the mean and RMS values over the replicas. The obtained values of the PDF parameters,  $\alpha_s$ , and  $m_t^{\text{pole}}$  and their fit uncertainties are in agreement with the nominal results.

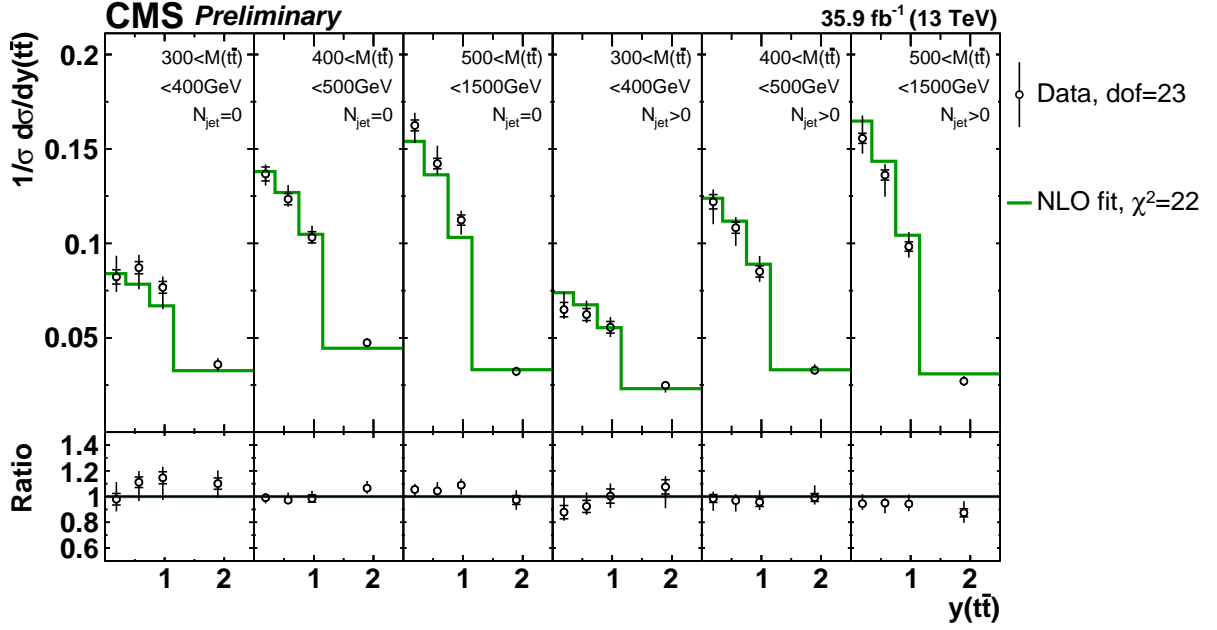


Figure 19: Comparison of the measured  $[N_{\text{jet}}^{0,1+}, M(t\bar{t}), y(t\bar{t})]$  cross sections to the NLO predictions using the parameter values from the simultaneous PDF,  $\alpha_s$  and  $m_t^{\text{pole}}$  fit. The inner vertical bars on the data points represent the statistical uncertainties and the full bars include also the systematic uncertainties added in quadrature. A  $\chi^2/\text{dof}$  is reported.

## 9.2 $\alpha_s$ and $m_t^{\text{pole}}$ extraction

The resulting values of  $\alpha_s$  and  $m_t^{\text{pole}}$  extracted using NLO calculations are:

$$\begin{aligned} \alpha_s(M_Z) &= 0.1135 \pm 0.0016(\text{fit})_{-0.0004}^{+0.0002}(\text{mod})_{-0.0001}^{+0.0008}(\text{par})_{-0.0005}^{+0.0011}(\text{scale}) = 0.1135_{-0.0017}^{+0.0021}(\text{total}), \\ m_t^{\text{pole}} &= 170.5 \pm 0.7(\text{fit})_{-0.1}^{+0.1}(\text{mod})_{-0.1}^{+0.0}(\text{par})_{-0.3}^{+0.3}(\text{scale}) \text{ GeV} = 170.5 \pm 0.8(\text{total}) \text{ GeV}. \end{aligned} \quad (7)$$

The uncertainties arising from the scale variations are estimated by repeating the fit with altered values of the scales as described in Section 8 and taking the differences with respect to the nominal result. The individual contributions to the uncertainties are listed in Table 2. The extracted  $\alpha_s$  and  $m_t^{\text{pole}}$  values have only weak positive correlation  $\rho(\alpha_s, m_t^{\text{pole}}) = 0.3$ , where the correlation was obtained from the data uncertainties propagated to the fit. This shows that the two SM parameters can be simultaneously determined from these data to high precision with only weak correlation between them.

The global and partial  $\chi^2$  values are listed in Table 3, illustrating the consistency of the input data with the fit model. In particular, the  $t\bar{t}$  data are well described in the fit. The DIS data show  $\chi^2/\text{dof}$  values slightly larger than unity, similar to what is observed and investigated in Ref. [86]. For the  $t\bar{t}$  data, the full  $\chi^2$  (including uncorrelated and correlated data uncertainties) is 22 for 23 dof. The  $t\bar{t}$  cross sections are compared to the NLO predictions obtained after the fit in Fig. 19.

Fits were performed for a series of  $\alpha_s(M_Z)$  values ranging from  $\alpha_s(M_Z) = 0.100$  to  $\alpha_s(M_Z) = 0.130$  using only HERA DIS data, or HERA and  $t\bar{t}$  data. The results are shown in Fig. 20. A shallow  $\chi^2$  dependence on  $\alpha_s(M_Z)$  is present when using only the HERA DIS data, similar to the findings of the HERAPDF2.0 analysis [86]. Once the  $t\bar{t}$  data are included in the fit, a distinct sharper minimum in  $\chi^2$  is observed which coincides with the one found in the simultaneous PDF and  $\alpha_s(M_Z)$  fit (Eq. 7).

Table 2: Central values and list of uncertainties for the  $\alpha_s$  and  $m_t^{\text{pole}}$  determination.

Parameter	Variation	$\alpha_s(M_Z)$	$m_t^{\text{pole}}$ [GeV]
Central value			
		0.1135	170.5
Fit uncertainty			
Total	$\Delta\chi^2 = 1$	$\pm 0.0016$	$\pm 0.7$
Model uncertainty			
$f_s$	$f_s = 0.5$	+0.0001	+0.0
$f_s$	$f_s = 0.3$	−0.0000	−0.0
$Q_{\min}^2$	$Q_{\min}^2 = 5.0 \text{ GeV}^2$	+0.0002	+0.1
$Q_{\min}^2$	$Q_{\min}^2 = 2.5 \text{ GeV}^2$	−0.0004	−0.1
$m_c$	$m_c = 1.49 \text{ GeV}$	+0.0001	+0.0
$m_c$	$m_c = 1.37 \text{ GeV}$	−0.0000	−0.0
Total		+0.0002 −0.0004	+0.1 −0.1
PDF parametrisation uncertainty			
$\mu_{f,0}^2$	$\mu_{f,0}^2 = 2.2 \text{ GeV}^2$	−0.0001	−0.0
$\mu_{f,0}^2$	$\mu_{f,0}^2 = 1.6 \text{ GeV}^2$	+0.0002	+0.0
$A'_g$	set to 0	+0.0002	−0.1
$E_g$	set to 0	+0.0008	−0.0
Total		+0.0008 −0.0001	+0.0 −0.1
Scale uncertainty			
$\mu_r$ variation	$\mu_r \times 2.0$	+0.0004	−0.2
$\mu_r$ variation	$\mu_r \times 0.5$	+0.0007	+0.1
$\mu_f$ variation	$\mu_f \times 2.0$	−0.0002	+0.3
$\mu_f$ variation	$\mu_f \times 0.5$	+0.0001	−0.3
$\mu_{r,f}$ variation	$\mu_{r,f} \times 2.0$	+0.0004	+0.1
$\mu_{r,f}$ variation	$\mu_{r,f} \times 0.5$	+0.0011	−0.2
alternative $\mu_{r,f}$	$\mu_{r,f} = H/2$	−0.0005	+0.1
Total		+0.0011 −0.0005	+0.3 −0.3

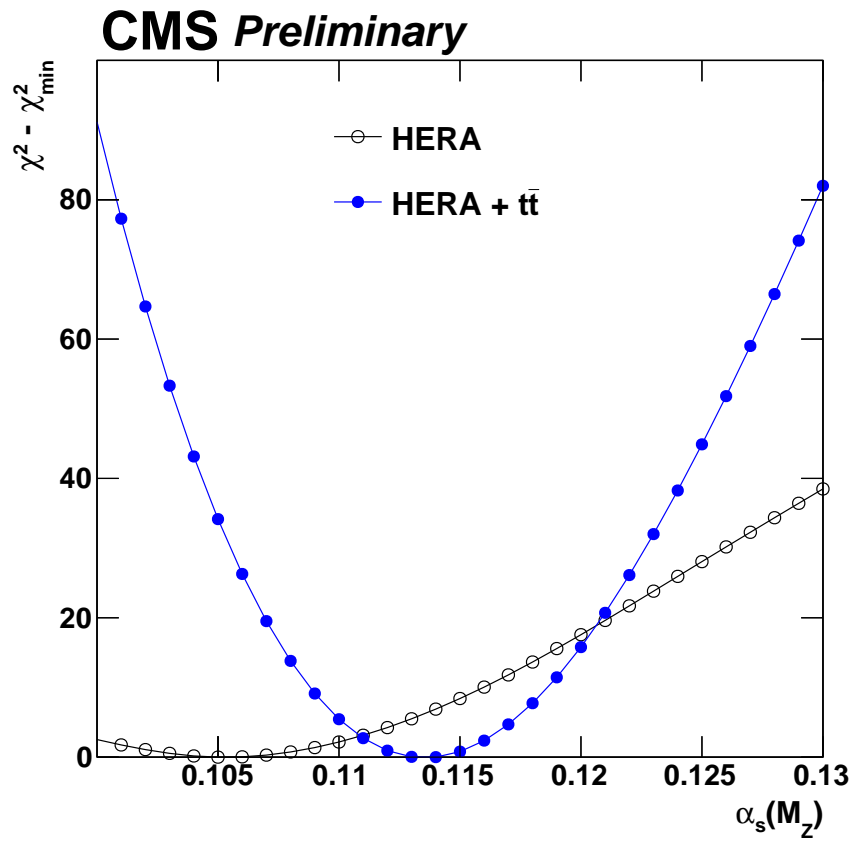


Figure 20:  $\Delta\chi^2 = \chi^2 - \chi_{\min}^2$  as a function of  $\alpha_s(M_Z)$  in the QCD analysis using the HERA DIS data only, or HERA and  $t\bar{t}$  data.

Table 3: The global and partial  $\chi^2/\text{dof}$  values for all variants of the QCD analysis. The variant of the fit that uses the HERA DIS only is denoted as ‘Nominal fit’. For the HERA measurements, the energy of the proton beam,  $E_p$ , is listed for each data set, with the electron energy being  $E_e = 27.5 \text{ GeV}$ , CC and NC stand for charged and neutral current, respectively. The correlated  $\chi^2$  and the log-penalty  $\chi^2$  entries refer to the  $\chi^2$  contributions from the nuisance parameters and from the logarithmic term, respectively, as described in the text.

Data sets	$\chi^2/\text{dof}$	
	Nominal fit	$+ [N_{\text{jet}}, y(\text{t}\bar{\text{t}}), M(\text{t}\bar{\text{t}})]$
CMS $\text{t}\bar{\text{t}}$		10/23
HERA CC $e^-p$ , $E_p = 920 \text{ GeV}$	55/42	55/42
HERA CC $e^+p$ , $E_p = 920 \text{ GeV}$	38/39	39/39
HERA NC $e^-p$ , $E_p = 920 \text{ GeV}$	218/159	217/159
HERA NC $e^+p$ , $E_p = 920 \text{ GeV}$	438/377	448/377
HERA NC $e^+p$ , $E_p = 820 \text{ GeV}$	70/70	71/70
HERA NC $e^+p$ , $E_p = 575 \text{ GeV}$	220/254	222/254
HERA NC $e^+p$ , $E_p = 460 \text{ GeV}$	219/204	220/204
Correlated $\chi^2$	82	90
Log-penalty $\chi^2$	+2	−7
Total $\chi^2/\text{dof}$	1341/1130	1364/1151

Both the  $\text{t}\bar{\text{t}}$  and the HERA DIS data are sensitive to the  $\alpha_s(M_Z)$  value in the fit: while the constraints from the  $\text{t}\bar{\text{t}}$  data seem to be dominant, the residual dependence of  $\alpha_s(M_Z)$  on the HERA DIS data may remain non-negligible. There is no way to assess the latter quantitatively because the HERA DIS data cannot be removed from the PDF fit. However, as was investigated in the HERAPDF2.0 analysis [86], when using only HERA DIS the minima are strongly dependent on the  $Q_{\text{min}}^2$  cut. As a cross check, the extraction of  $\alpha_s(M_Z)$  was repeated for a larger cut variation  $2.5 \leq Q_{\text{min}}^2 \leq 30.0 \text{ GeV}^2$ . In contrast to the results of Ref. [86] obtained using only HERA DIS data, when adding the  $\text{t}\bar{\text{t}}$  data the extracted values of  $\alpha_s(M_Z)$  show no systematic dependence on  $Q_{\text{min}}^2$  and are consistent with the nominal result of Eq. 7 within the total uncertainty.

The evolution of PDFs involves  $\alpha_s(M_Z)$ , therefore PDFs always depend on the  $\alpha_s(M_Z)$  assumed during their extraction. When using only the HERA DIS data, the largest dependence on  $\alpha_s(M_Z)$  is observed for the gluon distribution. The  $\text{t}\bar{\text{t}}$  data reduce this dependence, because they provide constraints on both the gluon distribution and  $\alpha_s(M_Z)$  reducing their correlation. This is illustrated in Fig.21 by plotting the gluon distribution at two different values  $x = 0.01$  and  $x = 0.1$  as a function of  $\alpha_s(M_Z)$  for the two variants of the fit. The chosen values of  $x$  represent the estimated boundaries of the sensitivity region of the  $\text{t}\bar{\text{t}}$  data. The  $\text{t}\bar{\text{t}}$  data greatly reduce the correlation between the gluon distribution and  $\alpha_s(M_Z)$ , especially at high  $x$ .

### 9.3 Impact of the $\text{t}\bar{\text{t}}$ cross section measurements on the PDF determination

To demonstrate the added value of the  $\text{t}\bar{\text{t}}$  cross sections, the QCD analysis is first performed using only the HERA DIS data. In this fit,  $\alpha_s$  is fixed to the value extracted from the fit using the  $\text{t}\bar{\text{t}}$  data,  $\alpha_s = 0.1135$ , and the  $\alpha_s$  uncertainty of  $\pm 0.0016$  is added to the fit uncertainties. Then the  $[N_{\text{jet}}^{0,1+}, M(\text{t}\bar{\text{t}}), y(\text{t}\bar{\text{t}})]$  measurement is added to the fit. The global and partial  $\chi^2$  values for the



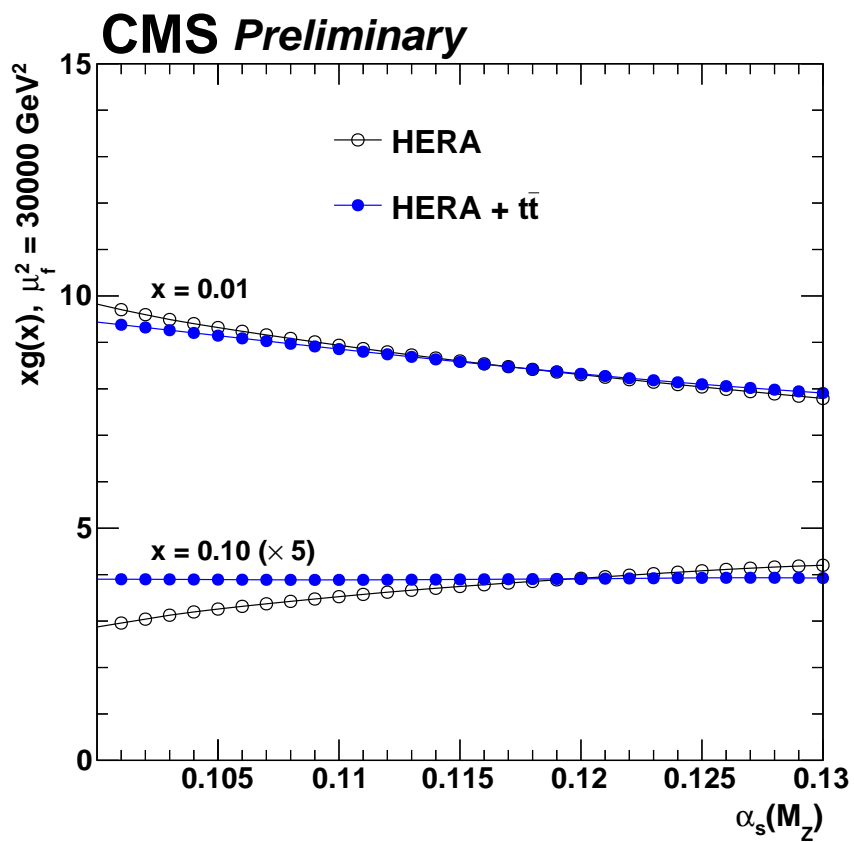


Figure 21: The gluon distribution  $xg(x)$  at the scale  $\mu_f^2 = 30000 \text{ GeV}^2$  for two values of  $x = 0.01$  and  $x = 0.1$  (the latter distribution is scaled by factor 5 for better visibility) as a function of  $\alpha_s(M_Z)$  in the QCD analysis using the HERA DIS data only, or HERA DIS and  $t\bar{t}$  data.

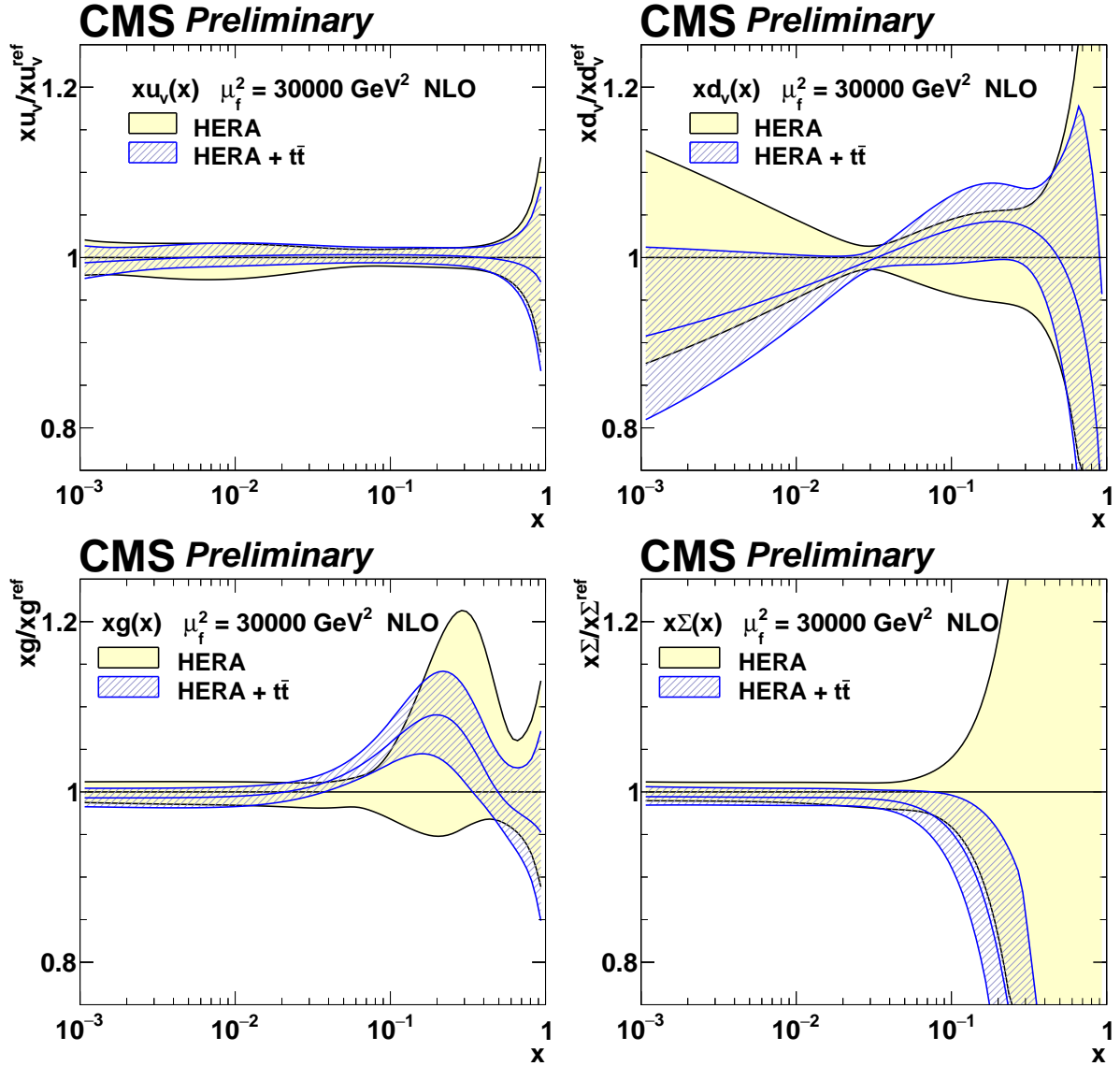


Figure 22: The PDFs with their total uncertainties in the fit using the HERA DIS data only, and the HERA DIS and  $t\bar{t}$  data. The results are normalised to the PDFs obtained using the HERA DIS data only.

two variants of the fit are listed in Table 3.

The corresponding PDFs are compared in Fig. 22. The largest impact of the  $t\bar{t}$  data is observed at  $x \gtrsim 0.1$ . In this region the gluon distribution lacks direct constraints in the fit using the HERA DIS data only.

In Fig. 23 the fit PDF uncertainties obtained from the fits using the HERA DIS data only, and HERA DIS and  $t\bar{t}$  data are compared. A reduction of uncertainties is observed for the gluon distribution, especially at  $x \sim 0.1$  where the included  $t\bar{t}$  data are expected to provide constraints, while the improvement at  $x \lesssim 0.1$  originates mainly from the reduced correlation between  $\alpha_s(M_Z)$  and the gluon (see Fig. 21). A smaller uncertainty reduction is observed for other PDFs as well (valence and sea quark distributions), which is expected because of the correlations between the different distributions in the fit arising in the PDF evolution and from the momentum sum rule. In Fig. 24 the total PDF uncertainties are shown for the two variants of the fits reveal-

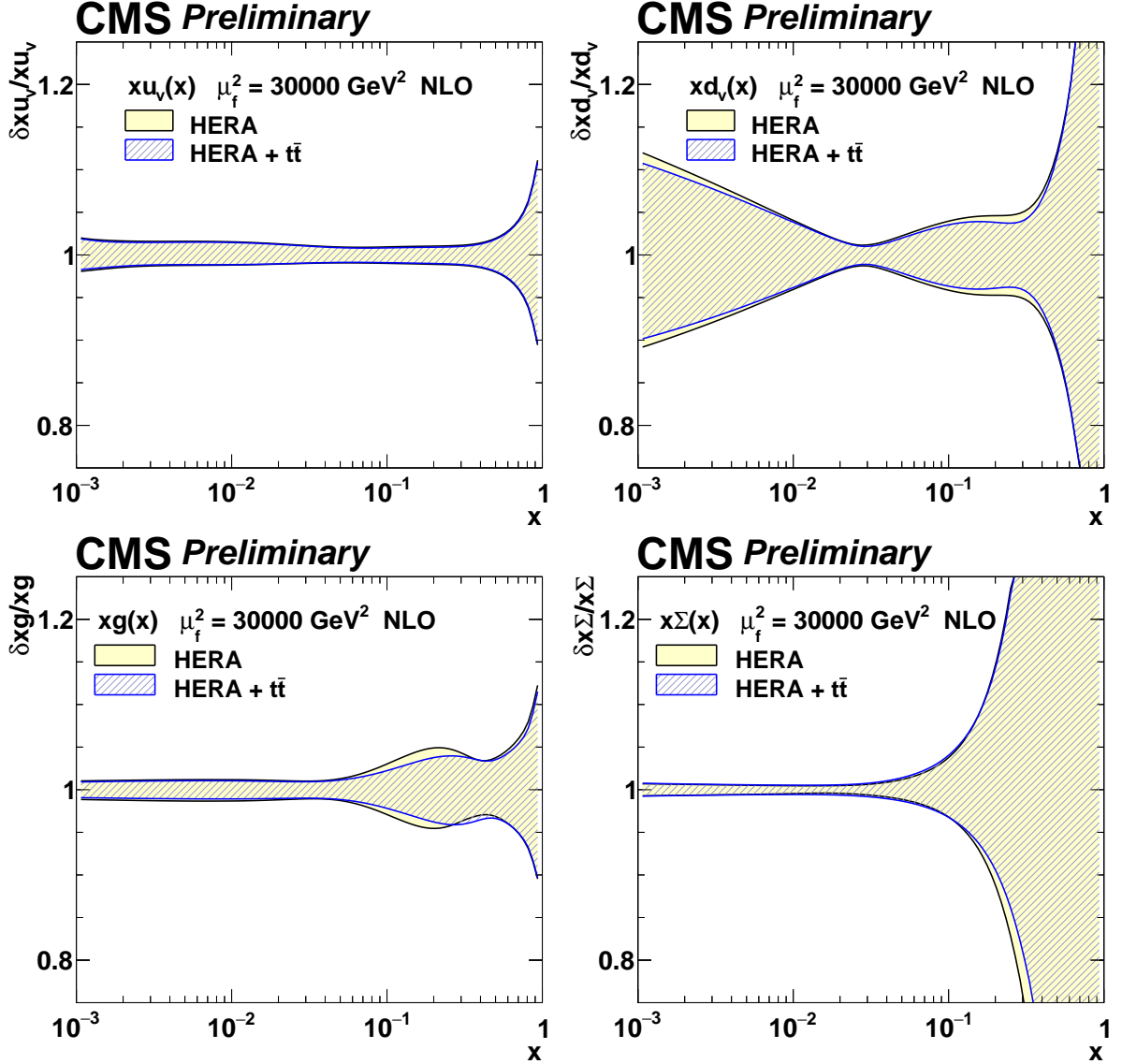


Figure 23: The relative total fit PDF uncertainties in the fit using the HERA DIS data only, and the HERA DIS and  $t\bar{t}$  data.

ing similar reduction of uncertainties after the inclusion of the  $t\bar{t}$  data into the fit. In addition to the fit uncertainty reduction, the  $t\bar{t}$  data constrain the large asymmetric model uncertainty of the gluon PDF at high  $x$  (propagated via the momentum sum rule to the uncertainty on the  $d_v$  at  $x \approx 0.01$ ). This uncertainty originates from the variation of  $Q_{\min}^2$  in the fit, using the HERA DIS data only, because of a lack of direct constraints from these data. The observed improvement makes future PDF fits at NNLO using the fully differential calculations [81, 82], once they become available in the format needed for such fits, very interesting.

## 10 Summary

A measurement of normalised multi-differential  $t\bar{t}$  production cross sections in pp collisions at  $\sqrt{s} = 13 \text{ TeV}$  has been presented. The measurement is performed using events containing two opposite-sign leptons (of electron or muon flavour). The analysed data were recorded in 2016 by the CMS detector at the LHC and correspond to an integrated luminosity of  $35.9 \text{ fb}^{-1}$ . The

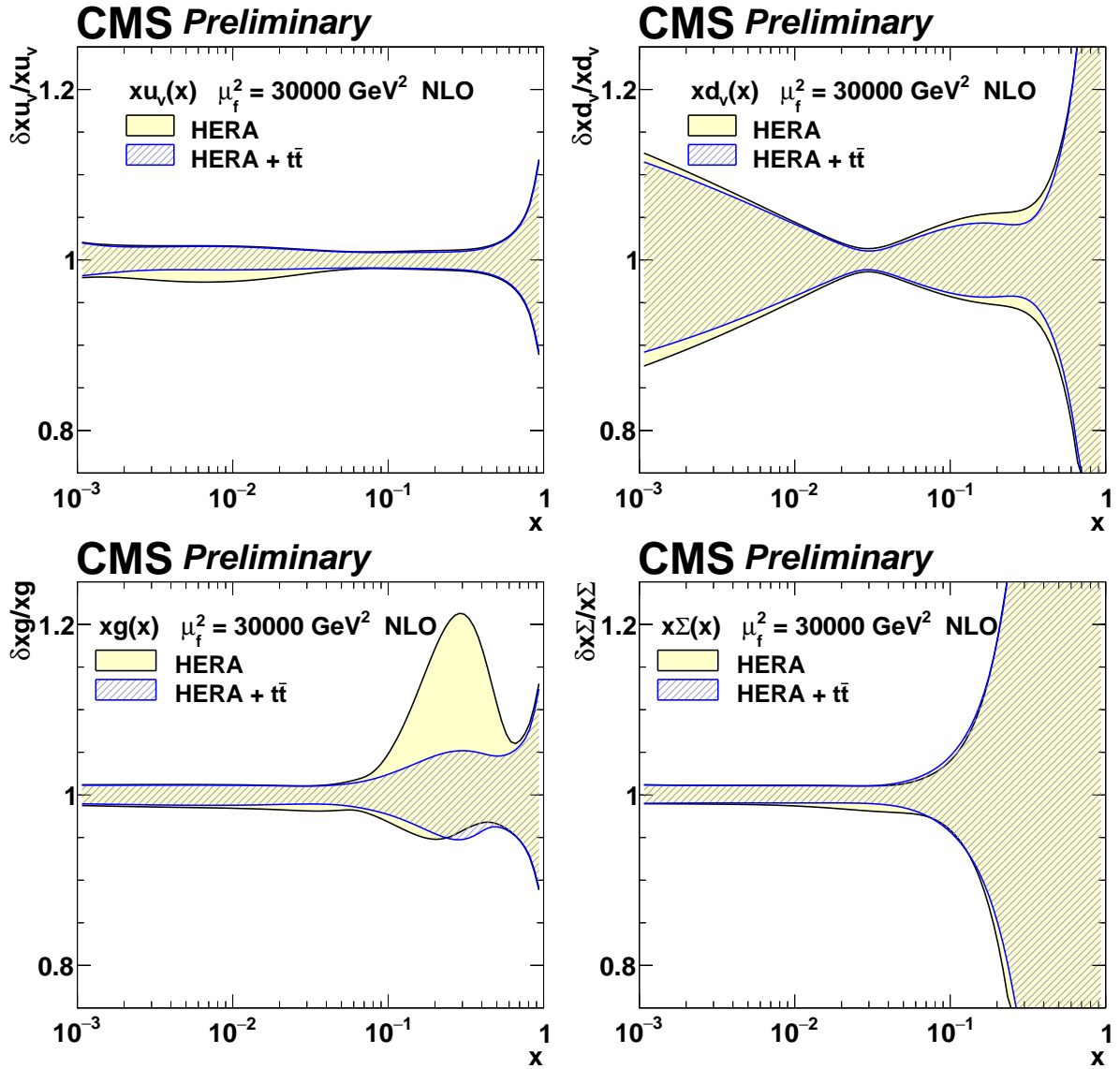


Figure 24: The relative total PDF uncertainties in the fit using the HERA DIS data only, and the HERA DIS and  $t\bar{t}$  data.

normalised  $t\bar{t}$  cross section is measured in the full phase space as a function of different pairs of kinematic variables describing the top quark or  $t\bar{t}$  system. None of the central predictions of the tested MC models is able to correctly describe all the distributions. The data exhibit a softer transverse momentum  $p_T(t)$  distribution, compared to the theoretical predictions, as was reported in previous single-differential and double-differential  $t\bar{t}$  cross section measurements. The effect of the softer  $p_T(t)$  spectrum with respect to the predictions is enhanced at larger values of  $M(t\bar{t})$ .

The measured  $t\bar{t}$  cross sections as a function of  $N_{\text{jet}}$ ,  $M(t\bar{t})$  and  $y(t\bar{t})$  have been incorporated into two specific fits of QCD parameters at NLO, after applying corrections for non-perturbative effects, together with the inclusive DIS data from HERA. When fitting only  $\alpha_s$  and  $m_t$  to the data, using external PDFs, the two parameters are determined with high accuracy and rather weak correlation between them, however the extracted  $\alpha_s$  values depends on the PDF set used. In a simultaneous fit of  $\alpha_s$  and  $m_t$  and PDFs the inclusion of the new multi-differential  $t\bar{t}$  measurements has a significant impact on the gluon PDF at large values of  $x$  and at the same time allows to accurately determine  $\alpha_s$  and  $m_t^{\text{pole}}$ .

## References

- [1] M. Czakon, M. L. Mangano, A. Mitov, and J. Rojo, “Constraints on the gluon PDF from top quark pair production at hadron colliders”, *JHEP* **07** (2013) 167, doi:10.1007/JHEP07(2013)167, arXiv:1303.7215.
- [2] M. Guzzi, K. Lipka, and S. Moch, “Top-quark pair production at hadron colliders: differential cross section and phenomenological applications with DIFFTOP”, *JHEP* **01** (2015) 082, doi:10.1007/JHEP01(2015)082, arXiv:1406.0386.
- [3] M. Czakon et al., “Pinning down the large- $x$  gluon with NNLO top-quark pair differential distributions”, *JHEP* **04** (2017) 044, doi:10.1007/JHEP04(2017)044, arXiv:1611.08609.
- [4] S. Alioli et al., “A new observable to measure the top-quark mass at hadron colliders”, *Eur. Phys. J. C* **73** (2013) 2438, doi:10.1140/epjc/s10052-013-2438-2, arXiv:1303.6415.
- [5] CDF Collaboration, “First measurement of the  $t\bar{t}$  differential cross section  $d\sigma/dM_{t\bar{t}}$  in  $p\bar{p}$  collisions at  $\sqrt{s} = 1.96$  TeV”, *Phys. Rev. Lett.* **102** (2009) 222003, doi:10.1103/PhysRevLett.102.222003, arXiv:0903.2850.
- [6] D0 Collaboration, “Measurement of differential  $t\bar{t}$  production cross sections in  $p\bar{p}$  collisions”, *Phys. Rev. D* **90** (2014) 092006, doi:10.1103/PhysRevD.90.092006, arXiv:1401.5785.
- [7] ATLAS Collaboration, “Measurements of top quark pair relative differential cross-sections with ATLAS in  $pp$  collisions at  $\sqrt{s} = 7$  TeV”, *Eur. Phys. J. C* **73** (2013) 2261, doi:10.1140/epjc/s10052-012-2261-1, arXiv:1207.5644.
- [8] CMS Collaboration, “Measurement of differential top-quark pair production cross sections in  $pp$  collisions at  $\sqrt{s} = 7$  TeV”, *Eur. Phys. J. C* **73** (2013) 2339, doi:10.1140/epjc/s10052-013-2339-4, arXiv:1211.2220.

- 
- [9] ATLAS Collaboration, “Measurements of normalized differential cross-sections for  $t\bar{t}$  production in pp collisions at  $\sqrt{s} = 7$  TeV using the ATLAS detector”, *Phys. Rev. D* **90** (2014) 072004, doi:10.1103/PhysRevD.90.072004, arXiv:1407.0371.
  - [10] ATLAS Collaboration, “Differential top-antitop cross-section measurements as a function of observables constructed from final-state particles using pp collisions at  $\sqrt{s} = 7$  TeV in the ATLAS detector”, *JHEP* **06** (2015) 100, doi:10.1007/JHEP06(2015)100, arXiv:1502.05923.
  - [11] ATLAS Collaboration, “Measurement of top quark pair differential cross-sections in the dilepton channel in pp collisions at  $\sqrt{s} = 7$  and 8 TeV with ATLAS”, *Phys. Rev. D* **94** (2016) 092003, doi:10.1103/PhysRevD.94.092003, arXiv:1607.07281.
  - [12] CMS Collaboration, “Measurement of the differential cross section for top quark pair production in pp collisions at  $\sqrt{s} = 8$  TeV”, *Eur. Phys. J. C* **75** (2015) 542, doi:10.1140/epjc/s10052-015-3709-x, arXiv:1505.04480.
  - [13] ATLAS Collaboration, “Measurements of top-quark pair differential cross-sections in the lepton+jets channel in pp collisions at  $\sqrt{s} = 8$  TeV using the ATLAS detector”, *Eur. Phys. J. C* **76** (2016) 538, doi:10.1140/epjc/s10052-016-4366-4, arXiv:1511.04716.
  - [14] ATLAS Collaboration, “Measurement of the differential cross-section of highly boosted top quarks as a function of their transverse momentum in  $\sqrt{s} = 8$  TeV proton-proton collisions using the ATLAS detector”, *Phys. Rev. D* **93** (2016) 032009, doi:10.1103/PhysRevD.93.032009, arXiv:1510.03818.
  - [15] CMS Collaboration, “Measurement of the  $t\bar{t}$  production cross section in the all-jets final state in pp collisions at  $\sqrt{s} = 8$  TeV”, *Eur. Phys. J. C* **76** (2016) 128, doi:10.1140/epjc/s10052-016-3956-5, arXiv:1509.06076.
  - [16] CMS Collaboration, “Measurement of the integrated and differential  $t\bar{t}$  production cross sections for high- $p_T$  top quarks in pp collisions at  $\sqrt{s} = 8$  TeV”, *Phys. Rev. D* **94** (2016) 072002, doi:10.1103/PhysRevD.94.072002, arXiv:1605.00116.
  - [17] CMS Collaboration, “Measurement of double-differential cross sections for top quark pair production in pp collisions at  $\sqrt{s} = 8$  TeV and impact on parton distribution functions”, *Eur. Phys. J. C* **77** (2017) 459, doi:10.1140/epjc/s10052-017-4984-5, arXiv:1703.01630.
  - [18] CMS Collaboration, “Measurement of differential cross sections for top quark pair production using the lepton+jets final state in proton-proton collisions at 13 TeV”, *Phys. Rev. D* **95** (2017), no. 9, 092001, doi:10.1103/PhysRevD.95.092001, arXiv:1610.04191.
  - [19] CMS Collaboration, “Measurement of differential cross sections for the production of top quark pairs and of additional jets in lepton+jets events from pp collisions at  $\sqrt{s} = 13$  TeV”, *Phys. Rev. D* **97** (2018), no. 11, 112003, doi:10.1103/PhysRevD.97.112003, arXiv:1803.08856.
  - [20] ATLAS Collaboration, “Measurement of jet activity produced in top-quark events with an electron, a muon and two b-tagged jets in the final state in pp collisions at  $\sqrt{s} = 13$  TeV with the ATLAS detector”, *Eur. Phys. J. C* **77** (2017) 220, doi:10.1140/epjc/s10052-017-4766-0, arXiv:1610.09978.

- [21] ATLAS Collaboration, “Measurements of top-quark pair differential cross-sections in the  $e\mu$  channel in pp collisions at  $\sqrt{s} = 13$  TeV using the ATLAS detector”, *Eur. Phys. J. C* **77** (2017) 292, doi:10.1140/epjc/s10052-017-4821-x, arXiv:1612.05220.
- [22] CMS Collaboration, “Measurement of normalized differential  $t\bar{t}$  cross sections in the dilepton channel from pp collisions at  $\sqrt{s} = 13$  TeV”, *JHEP* **04** (2018) 060, doi:10.1007/JHEP04(2018)060, arXiv:1708.07638.
- [23] CMS Collaboration, “Measurements of  $t\bar{t}$  differential cross sections in proton-proton collisions at  $\sqrt{s} = 13$  TeV using events containing two leptons”, arXiv:1811.06625. Submitted to JHEP.
- [24] CMS Collaboration, “Measurement of  $t\bar{t}$  production with additional jet activity, including b quark jets, in the dilepton decay channel using pp collisions at  $\sqrt{s} = 8$  TeV”, *Eur. Phys. J. C* **76** (2016) 379, doi:10.1140/epjc/s10052-016-4105-x, arXiv:1510.03072.
- [25] ATLAS Collaboration, “Measurement of jet activity in top quark events using the  $e\mu$  final state with two b-tagged jets in pp collisions at  $\sqrt{s} = 8$  TeV with the ATLAS detector”, *JHEP* **09** (2016) 074, doi:10.1007/JHEP09(2016)074, arXiv:1606.09490.
- [26] D0 Collaboration, “Determination of the pole and  $\overline{MS}$  masses of the top quark from the  $t\bar{t}$  cross section”, *Phys. Lett. B* **703** (2011) 422–427, doi:10.1016/j.physletb.2011.08.015, arXiv:1104.2887.
- [27] CMS Collaboration, “Determination of the top-quark pole mass and strong coupling constant from the  $t\bar{t}$  production cross section in pp collisions at  $\sqrt{s} = 7$  TeV”, *Phys. Lett. B* **728** (2014) 496–517, doi:10.1016/j.physletb.2014.08.040, 10.1016/j.physletb.2013.12.009, arXiv:1307.1907. [Erratum: *Phys. Lett. B* **738**, 526(2014)].
- [28] ATLAS Collaboration, “Measurement of the  $t\bar{t}$  production cross-section using  $e\mu$  events with b-tagged jets in pp collisions at  $\sqrt{s} = 7$  and 8 TeV with the ATLAS detector”, *Eur. Phys. J. C* **74** (2014), no. 10, 3109, doi:10.1140/epjc/s10052-016-4501-2, 10.1140/epjc/s10052-014-3109-7, arXiv:1406.5375. [Addendum: *Eur. Phys. J. C* **76**, no. 11, 642(2016)].
- [29] D0 Collaboration, “Measurement of the Inclusive  $t\bar{t}$  Production Cross Section in  $p\bar{p}$  Collisions at  $\sqrt{s} = 1.96$  TeV and Determination of the Top Quark Pole Mass”, *Phys. Rev. D* **94** (2016) 092004, doi:10.1103/PhysRevD.94.092004, arXiv:1605.06168.
- [30] CMS Collaboration, “Measurement of the  $t\bar{t}$  production cross section in the  $e\mu$  channel in proton-proton collisions at  $\sqrt{s} = 7$  and 8 TeV”, *JHEP* **08** (2016) 029, doi:10.1007/JHEP08(2016)029, arXiv:1603.02303.
- [31] CMS Collaboration, “Measurement of the  $t\bar{t}$  production cross section, the top quark mass, and the strong coupling constant using events in the dilepton final state in pp collisions at  $\sqrt{s} = 13$  TeV”, CMS Physics Analysis Summary CMS-PAS-TOP-17-001, 2018.
- [32] S. Frixione, P. Nason, and C. Oleari, “Matching NLO QCD computations with parton shower simulations: the POWHEG method”, *JHEP* **11** (2007) 070, doi:10.1088/1126-6708/2007/11/070, arXiv:0709.2092.

- 
- [33] E. Re, “Single-top Wt-channel production matched with parton showers using the POWHEG method”, *Eur. Phys. J. C* **71** (2011) 1547, doi:10.1140/epjc/s10052-011-1547-z, arXiv:1009.2450.
- [34] J. Alwall et al., “The automated computation of tree-level and next-to-leading order differential cross sections, and their matching to parton shower simulations”, *JHEP* **07** (2014) 079, doi:10.1007/JHEP07(2014)079, arXiv:1405.0301.
- [35] T. Sjöstrand, S. Mrenna, and P. Z. Skands, “PYTHIA 6.4 Physics and Manual”, *JHEP* **05** (2006) 026, doi:10.1088/1126-6708/2006/05/026, arXiv:hep-ph/0603175.
- [36] T. Sjöstrand et al., “An introduction to PYTHIA 8.2”, *Comput. Phys. Commun.* **191** (2015) 159, doi:10.1016/j.cpc.2015.01.024, arXiv:1410.3012.
- [37] NNPDF Collaboration, “Unbiased global determination of parton distributions and their uncertainties at NNLO and LO”, *Nucl. Phys. B* **855** (2012) 153, doi:10.1016/j.nuclphysb.2011.09.024, arXiv:1107.2652.
- [38] S. Frixione, P. Nason, and G. Ridolfi, “A positive-weight next-to-leading-order Monte Carlo for heavy flavour hadroproduction”, *JHEP* **09** (2007) 126, doi:10.1088/1126-6708/2007/09/126, arXiv:0707.3088.
- [39] S. Alioli et al., “A general framework for implementing NLO calculations in shower Monte Carlo programs: the POWHEG BOX”, *JHEP* **06** (2010) 043, doi:10.1007/JHEP06(2010)043, arXiv:1002.2581.
- [40] CMS Collaboration, “Investigations of the impact of the parton shower tuning in PYTHIA8 in the modelling of  $t\bar{t}$  at  $\sqrt{s} = 8$  and 13 TeV”, CMS Physics Analysis Summary CMS-PAS-TOP-16-021, 2016.
- [41] CMS Collaboration, “Underlying event tunes and double parton scattering”, CMS Physics Analysis Summary CMS-PAS-GEN-14-001, 2014.
- [42] P. Skands, S. Carrazza, and J. Rojo, “Tuning PYTHIA 8.1: the Monash 2013 Tune”, *Eur. Phys. J. C* **74** (2014), no. 8, 3024, doi:10.1140/epjc/s10052-014-3024-y, arXiv:1404.5630.
- [43] P. Artoisenet et al., “Automatic spin-entangled decays of heavy resonances in Monte Carlo simulations”, *JHEP* **03** (2013) 015, doi:10.1007/JHEP03(2013)015, arXiv:1212.3460.
- [44] R. Frederix and S. Frixione, “Merging meets matching in MC@NLO”, *JHEP* **12** (2012) 061, doi:10.1007/JHEP12(2012)061, arXiv:1209.6215.
- [45] M. Bahr et al., “Herwig++ Physics and Manual”, *Eur. Phys. J. C* **58** (2008) 639–707, doi:10.1140/epjc/s10052-008-0798-9, arXiv:0803.0883.
- [46] M. H. Seymour and A. Siodmok, “Constraining MPI models using  $\sigma_{eff}$  and recent Tevatron and LHC underlying event data”, *JHEP* **10** (2013) 113, doi:10.1007/JHEP10(2013)113, arXiv:1307.5015.
- [47] S. Alioli et al., “NLO single-top production matched with shower in POWHEG: s- and t-channel contributions”, *JHEP* **09** (2009) 111, doi:10.1088/1126-6708/2009/09/111, arXiv:0907.4076.



- [48] J. Alwall et al., “Comparative study of various algorithms for the merging of parton showers and matrix elements in hadronic collisions”, *Eur. Phys. J. C* **53** (2008) 437, doi:10.1140/epjc/s10052-007-0490-5, arXiv:0706.2569.
- [49] N. Kidonakis, “Two-loop soft anomalous dimensions for single top quark associated production with  $W^-$  or  $H^-$ ”, *Phys. Rev. D* **82** (2010) 054018, doi:10.1103/PhysRevD.82.054018, arXiv:hep-ph/1005.4451.
- [50] Y. Li and F. Petriello, “Combining QCD and electroweak corrections to dilepton production in FEWZ”, *Phys. Rev. D* **86** (2012) 094034, doi:10.1103/PhysRevD.86.094034, arXiv:1208.5967.
- [51] J. M. Campbell, R. K. Ellis, and C. Williams, “Vector boson pair production at the LHC”, *JHEP* **07** (2011) 018, doi:10.1007/JHEP07(2011)018, arXiv:1105.0020.
- [52] M. Czakon and A. Mitov, “Top++: A Program for the Calculation of the Top-Pair Cross-Section at Hadron Colliders”, *Comput.Phys.Commun.* **185** (2014) 2930, doi:10.1016/j.cpc.2014.06.021, arXiv:1112.5675.
- [53] GEANT4 Collaboration, “GEANT4—a simulation toolkit”, *Nucl. Instrum. Meth. A* **506** (2003) 250, doi:10.1016/S0168-9002(03)01368-8.
- [54] CMS Collaboration, “Particle-flow reconstruction and global event description with the CMS detector”, *JINST* **12** (2017) P10003, doi:10.1088/1748-0221/12/10/P10003, arXiv:1706.04965.
- [55] M. Cacciari, G. P. Salam, and G. Soyez, “The catchment area of jets”, *JHEP* **04** (2008) 005, doi:10.1088/1126-6708/2008/04/005, arXiv:0802.1188.
- [56] CMS Collaboration, “Performance of electron reconstruction and selection with the CMS detector in proton-proton collisions at  $\sqrt{s} = 8$  TeV”, *JINST* **10** (2015) P06005, doi:10.1088/1748-0221/10/06/P06005, arXiv:1502.02701.
- [57] M. Cacciari, G. P. Salam, and G. Soyez, “The anti- $k_t$  jet clustering algorithm”, *JHEP* **04** (2008) 063, doi:10.1088/1126-6708/2008/04/063, arXiv:0802.1189.
- [58] M. Cacciari, G. P. Salam, and G. Soyez, “FastJet user manual”, *Eur. Phys. J. C* **72** (2012) 1896, doi:10.1140/epjc/s10052-012-1896-2, arXiv:1111.6097.
- [59] CMS Collaboration, “Jet energy scale and resolution in the CMS experiment in pp collisions at 8 TeV”, *JINST* **12** (2017) P02014, doi:10.1088/1748-0221/12/02/P02014, arXiv:1607.03663.
- [60] CMS Collaboration, “Identification of heavy-flavour jets with the CMS detector in pp collisions at 13 TeV”, *JINST* **13** (2018), no. 05, P05011, doi:10.1088/1748-0221/13/05/P05011, arXiv:1712.07158.
- [61] Review of Particle Physics, C. Patrignani et al. *Chin. Phys.* **C40** (2016) 100001, doi:10.1088/1674-1137/40/10/100001.
- [62] S. Schmitt, “TUnfold: an algorithm for correcting migration effects in high energy physics”, *JINST* **7** (2012) T10003, doi:10.1088/1748-0221/7/10/T10003, arXiv:1205.6201.

- 
- [63] A. N. Tikhonov, "Solution of incorrectly formulated problems and the regularization method", *Soviet Math. Dokl.* **4** (1963) 1035.
  - [64] S. Schmitt, "Data Unfolding Methods in High Energy Physics", *EPJ Web Conf.* **137** (2017) 11008, doi:10.1051/epjconf/201713711008, arXiv:1611.01927.
  - [65] Particle Data Group, M. Tanabashi et al. *Phys. Rev.* **D98** (2018), no. 3, 030001, doi:10.1103/PhysRevD.98.030001.
  - [66] ATLAS Collaboration, "Measurement of the inelastic proton-proton cross section at  $\sqrt{s} = 13$  TeV with the ATLAS detector at the LHC", *Phys. Rev. Lett.* **117** (2016) 182002, doi:10.1103/PhysRevLett.117.182002, arXiv:1606.02625.
  - [67] CMS Collaboration, "Measurement of the Drell-Yan cross section in pp collisions at  $\sqrt{s} = 7$  TeV", *JHEP* **10** (2011) 007, doi:10.1007/JHEP10(2011)007, arXiv:1108.0566.
  - [68] CMS Collaboration, "Measurement of the top quark pair production cross section in proton-proton collisions at  $\sqrt{s} = 13$  TeV", *Phys. Rev. Lett.* **116** (2016), no. 5, 052002, doi:10.1103/PhysRevLett.116.052002, arXiv:1510.05302.
  - [69] CMS Collaboration, "Jet energy scale and resolution in the CMS experiment in pp collisions at 8 TeV", *JINST* **12** (2017), no. 02, P02014, doi:10.1088/1748-0221/12/02/P02014, arXiv:1607.03663.
  - [70] CMS Collaboration, "CMS luminosity measurements for the 2016 data taking period", Technical Report CMS-PAS-LUM-17-001, CERN, Geneva, 2017.
  - [71] S. Dulat et al., "New parton distribution functions from a global analysis of quantum chromodynamics", *Phys. Rev.* **D93** (2016), no. 3, 033006, doi:10.1103/PhysRevD.93.033006, arXiv:1506.07443.
  - [72] S. Argyropoulos and T. Sjöstrand, "Effects of color reconnection on  $t\bar{t}$  final states at the LHC", *JHEP* **11** (2014) 043, doi:10.1007/JHEP11(2014)043, arXiv:1407.6653.
  - [73] J. R. Christiansen and P. Z. Skands, "String formation beyond leading colour", *JHEP* **08** (2015) 003, doi:10.1007/JHEP08(2015)003, arXiv:1505.01681.
  - [74] M. G. Bowler, " $e^+e^-$  Production of Heavy Quarks in the String Model", *Z. Phys.* **C11** (1981) 169, doi:10.1007/BF01574001.
  - [75] C. Peterson, D. Schlatter, I. Schmitt, and P. M. Zerwas, "Scaling violations in inclusive  $e^+e^-$  annihilation spectra", *Phys. Rev. D* **27** (1983) 105, doi:10.1103/PhysRevD.27.105.
  - [76] M. L. Mangano, P. Nason, and G. Ridolfi, "Heavy quark correlations in hadron collisions at next-to-leading order", *Nucl. Phys. B* **373** (1992) 295, doi:10.1016/0550-3213(92)90435-E.
  - [77] S. Dittmaier, P. Uwer, and S. Weinzierl, "NLO QCD corrections to  $t\bar{t}$  + jet production at hadron colliders", *Phys. Rev. Lett.* **98** (2007) 262002, doi:10.1103/PhysRevLett.98.262002, arXiv:hep-ph/0703120.

- [78] G. Bevilacqua, M. Czakon, C. G. Papadopoulos, and M. Worek, “Dominant QCD Backgrounds in Higgs Boson Analyses at the LHC: A Study of  $pp \rightarrow t\bar{t} + 2$  jets at Next-To-Leading Order”, *Phys. Rev. Lett.* **104** (2010) 162002, doi:10.1103/PhysRevLett.104.162002, arXiv:1002.4009.
- [79] G. Bevilacqua, M. Czakon, C. G. Papadopoulos, and M. Worek, “Hadronic top-quark pair production in association with two jets at Next-to-Leading Order QCD”, *Phys. Rev. D* **84** (2011) 114017, doi:10.1103/PhysRevD.84.114017, arXiv:1108.2851.
- [80] S. Höche et al., “Next-to-leading order QCD predictions for top-quark pair production with up to three jets”, *Eur. Phys. J. C* **77** (2017) 145, doi:10.1140/epjc/s10052-017-4715-y, arXiv:1607.06934.
- [81] M. Czakon, D. Heymes, and A. Mitov, “High-precision differential predictions for top-quark pairs at the LHC”, *Phys. Rev. Lett.* **116** (2016) 082003, doi:10.1103/PhysRevLett.116.082003, arXiv:1511.00549.
- [82] M. Czakon, D. Heymes, and A. Mitov, “Dynamical scales for multi-TeV top-pair production at the LHC”, *JHEP* **04** (2017) 071, doi:10.1007/JHEP04(2017)071, arXiv:1606.03350.
- [83] S. Alekhin, J. Blümlein, and S. Moch, “NLO PDFs from the ABMP16 fit”, *Eur. Phys. J. C* **78** (2018), no. 6, 477, doi:10.1140/epjc/s10052-018-5947-1, arXiv:1803.07537.
- [84] A. Accardi et al., “Constraints on large- $x$  parton distributions from new weak boson production and deep-inelastic scattering data”, *Phys. Rev. D* **93** (2016) 114017, doi:10.1103/PhysRevD.93.114017, arXiv:1602.03154.
- [85] S. Dulat et al., “New parton distribution functions from a global analysis of quantum chromodynamics”, *Phys. Rev. D* **93** (2016) 033006, doi:10.1103/PhysRevD.93.033006, arXiv:1506.07443.
- [86] H1 and ZEUS Collaborations, “Combination of measurements of inclusive deep inelastic  $e^+p$  scattering cross sections and QCD analysis of HERA data”, *Eur. Phys. J. C* **75** (2015) 580, doi:10.1140/epjc/s10052-015-3710-4, arXiv:1506.06042.
- [87] P. Jimenez-Delgado and E. Reya, “Delineating parton distributions and the strong coupling”, *Phys. Rev. D* **89** (2014) 074049, doi:10.1103/PhysRevD.89.074049, arXiv:1403.1852.
- [88] L. A. Harland-Lang, A. D. Martin, P. Motylinski, and R. S. Thorne, “Parton distributions in the LHC era: MMHT 2014 PDFs”, *Eur. Phys. J. C* **75** (2015) 204, doi:10.1140/epjc/s10052-015-3397-6, arXiv:1412.3989.
- [89] NNPDF Collaboration, “Parton distributions from high-precision collider data”, *Eur. Phys. J. C* **77** (2017), no. 10, 663, doi:10.1140/epjc/s10052-017-5199-5, arXiv:1706.00428.
- [90] A. Buckley et al., “LHAPDF6: parton density access in the LHC precision era”, *Eur. Phys. J. C* **75** (2015) 132, doi:10.1140/epjc/s10052-015-3318-8, arXiv:1412.7420.
- [91] M. Cacciari et al., “Updated predictions for the total production cross sections of top and of heavier quark pairs at the Tevatron and at the LHC”, *JHEP* **09** (2008) 127, doi:10.1088/1126-6708/2008/09/127, arXiv:0804.2800.

- 
- [92] Y. Kiyo et al., “Top-quark pair production near threshold at LHC”, *Eur. Phys. J.* **C60** (2009) 375–386, doi:10.1140/epjc/s10052-009-0892-7, arXiv:0812.0919.
- [93] J. H. Kühn, A. Scharf, and P. Uwer, “Weak Interactions in Top-Quark Pair Production at Hadron Colliders: An Update”, *Phys. Rev.* **D91** (2015), no. 1, 014020, doi:10.1103/PhysRevD.91.014020, arXiv:1305.5773.
- [94] M. Czakon et al., “Top-pair production at the LHC through NNLO QCD and NLO EW”, *JHEP* **10** (2017) 186, doi:10.1007/JHEP10(2017)186, arXiv:1705.04105.
- [95] S. Alekhin et al., “HERAFitter”, *Eur. Phys. J. C* **75** (2015) 304, doi:10.1140/epjc/s10052-015-3480-z, arXiv:1410.4412. xFITTER web site, <https://www.xfitter.org>.
- [96] Y. L. Dokshitzer, “Calculation of the structure functions for deep inelastic scattering and  $e^+e^-$  annihilation by perturbation theory in quantum chromodynamics”, *Sov. Phys. JETP* **46** (1977) 641.
- [97] V. N. Gribov and L. N. Lipatov, “Deep inelastic ep scattering in perturbation theory”, *Sov. J. Nucl. Phys.* **15** (1972) 438.
- [98] G. Altarelli and G. Parisi, “Asymptotic freedom in parton language”, *Nucl. Phys. B* **126** (1977) 298, doi:10.1016/0550-3213(77)90384-4.
- [99] G. Curci, W. Furmanski, and R. Petronzio, “Evolution of parton densities beyond leading order: the nonsinglet case”, *Nucl. Phys. B* **175** (1980) 27, doi:10.1016/0550-3213(80)90003-6.
- [100] W. Furmanski and R. Petronzio, “Singlet parton densities beyond leading order”, *Phys. Lett. B* **97** (1980) 437, doi:10.1016/0370-2693(80)90636-X.
- [101] S. Moch, J. A. M. Vermaseren, and A. Vogt, “The three-loop splitting functions in QCD: the nonsinglet case”, *Nucl. Phys. B* **688** (2004) 101, doi:10.1016/j.nuclphysb.2004.03.030, arXiv:hep-ph/0403192.
- [102] A. Vogt, S. Moch, and J. A. M. Vermaseren, “The three-loop splitting functions in QCD: the singlet case”, *Nucl. Phys. B* **691** (2004) 129, doi:10.1016/j.nuclphysb.2004.04.024, arXiv:hep-ph/0404111.
- [103] M. Botje, “QCDNUM: Fast QCD evolution and convolution”, *Comput. Phys. Commun.* **182** (2011) 490, doi:10.1016/j.cpc.2010.10.020, arXiv:1005.1481.
- [104] R. S. Thorne and R. G. Roberts, “An ordered analysis of heavy flavor production in deep inelastic scattering”, *Phys. Rev. D* **57** (1998) 6871, doi:10.1103/PhysRevD.57.6871, arXiv:hep-ph/9709442.
- [105] R. S. Thorne, “A variable-flavor number scheme for NNLO”, *Phys. Rev. D* **73** (2006) 054019, doi:10.1103/PhysRevD.73.054019, arXiv:hep-ph/0601245.
- [106] R. S. Thorne, “Effect of changes of variable flavor number scheme on parton distribution functions and predicted cross sections”, *Phys. Rev. D* **86** (2012) 074017, doi:10.1103/PhysRevD.86.074017, arXiv:1201.6180.
- [107] V. Bertone et al., “aMCfast: automation of fast NLO computations for PDF fits”, *JHEP* **08** (2014) 166, doi:10.1007/JHEP08(2014)166, arXiv:1406.7693.

- [108] T. Carli et al., “A posteriori inclusion of parton density functions in NLO QCD final-state calculations at hadron colliders: The APPLGRID project”, *Eur. Phys. J. C* **66** (2010) 503, doi:10.1140/epjc/s10052-010-1255-0, arXiv:0911.2985.
- [109] A. D. Martin, W. J. Stirling, R. S. Thorne, and G. Watt, “Parton distributions for the LHC”, *Eur. Phys. J. C* **63** (2009) 189, doi:10.1140/epjc/s10052-009-1072-5, arXiv:0901.0002.
- [110] CMS Collaboration, “Measurement of the muon charge asymmetry in inclusive  $pp \rightarrow W + X$  production at  $\sqrt{s} = 7$  TeV and an improved determination of light parton distribution functions”, *Phys. Rev. D* **90** (2014) 032004, doi:10.1103/PhysRevD.90.032004, arXiv:1312.6283.
- [111] H1 Collaboration, “Inclusive deep inelastic scattering at high  $Q^2$  with longitudinally polarised lepton beams at HERA”, *JHEP* **09** (2012) 061, doi:10.1007/JHEP09(2012)061, arXiv:1206.7007.
- [112] W. T. Giele and S. Keller, “Implications of hadron collider observables on parton distribution function uncertainties”, *Phys. Rev. D* **58** (1998) 094023, doi:10.1103/PhysRevD.58.094023, arXiv:hep-ph/9803393.
- [113] W. T. Giele, S. A. Keller, and D. A. Kosower, “Parton distribution function uncertainties”, arXiv:hep-ph/0104052.

## A Additional details and plots for $\alpha_s$ and $m_t^{\text{pole}}$ extraction using external PDFs

The  $\alpha_s$  scans performed using altered scale and  $m_t^{\text{pole}}$  settings and CT14, HERAPDF2.0 and ABMP16 PDF sets are shown in Fig. 25.

The  $m_t^{\text{pole}}$  scans for the same variations are shown in Fig. 26.

The extracted values of  $\alpha_s$  and  $m_t^{\text{pole}}$  obtained using single-differential cross sections as a function of  $N_{\text{jet}}$ ,  $M(t\bar{t})$  and  $y(t\bar{t})$  are shown in Fig. 27.

### A.1 $\alpha_s$ and $m_t^{\text{pole}}$ extraction using $[p_T(t\bar{t}), M(t\bar{t}), y(t\bar{t})]$ cross sections with two $p_T(t\bar{t})$ bins.

The NLO calculations for inclusive  $t\bar{t}$  and  $t\bar{t} + 1$  jet production with an appropriate jet  $p_T$  threshold are used to describe the distribution in the two  $p_T(t\bar{t})$  bins. Because the final state of the NLO calculation for  $t\bar{t}$  and at least one jet consists of maximum two light partons, there can be up to two jets built of these partons, which balance the transverse momentum of  $t\bar{t}$ . Therefore e.g. for  $p_T(t\bar{t}) > 100$  GeV there is at least one jet with  $p_T > 50$  GeV in the NLO calculation, and one can use the  $t\bar{t} + 1$  jet calculation requiring  $p_T(t\bar{t}) > 100$  GeV without any requirement of the extra jet (if the jet  $p_T$  threshold is not larger than 50 GeV). In this analysis, the jet  $p_T > 30$  GeV was found to correspond approximately to  $p_T(t\bar{t}) \gtrsim 50$  GeV, therefore the boundary of 50 GeV was chosen to split the data into two  $p_T(t\bar{t})$  bins. The minimum jet  $p_T$  of 15 GeV was used in the NLO calculation for inclusive  $t\bar{t} + 1$  jet production (no cut on jet  $|\eta|$ ), and the predicted events were required to have  $p_T(t\bar{t}) > 50$  GeV. This calculation was used for the bin with  $p_T(t\bar{t}) > 50$  GeV, while for the bin with  $p_T(t\bar{t}) < 50$  GeV the difference of the predictions for inclusive  $t\bar{t}$  production and inclusive  $t\bar{t} + 1$  jet production was used. The extracted values of  $\alpha_s$  and  $m_t^{\text{pole}}$

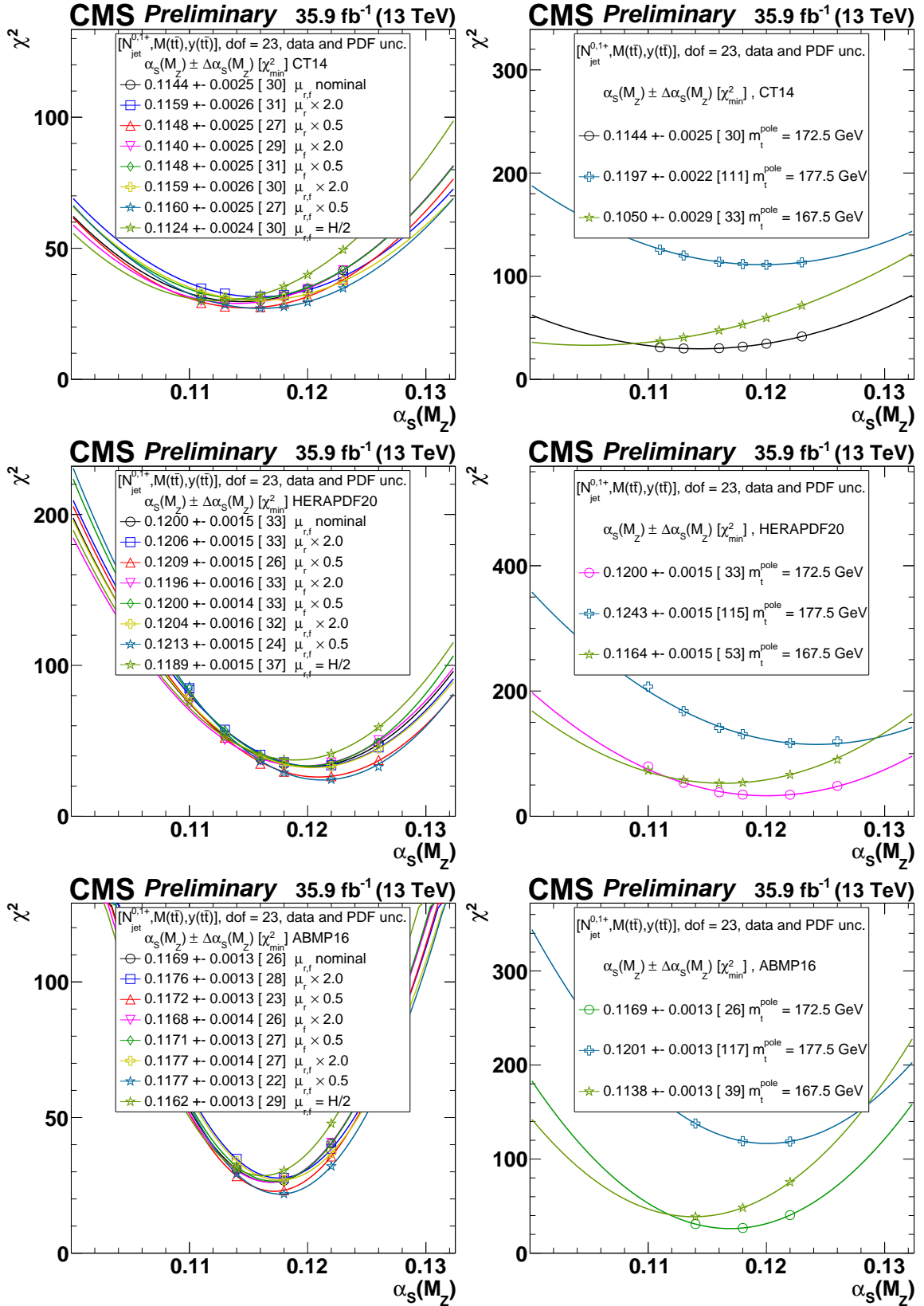


Figure 25: The  $\alpha_s$  extraction from the measured  $[N_{\text{jet}}^{0,1+}, M(t\bar{t}), y(t\bar{t})]$  cross sections using varied scale and  $m_t$  settings and CT14 (top), HERAPDF2.0 (middle) and ABMP16 (bottom) PDF sets. Details can be found in the caption of Fig. 17.

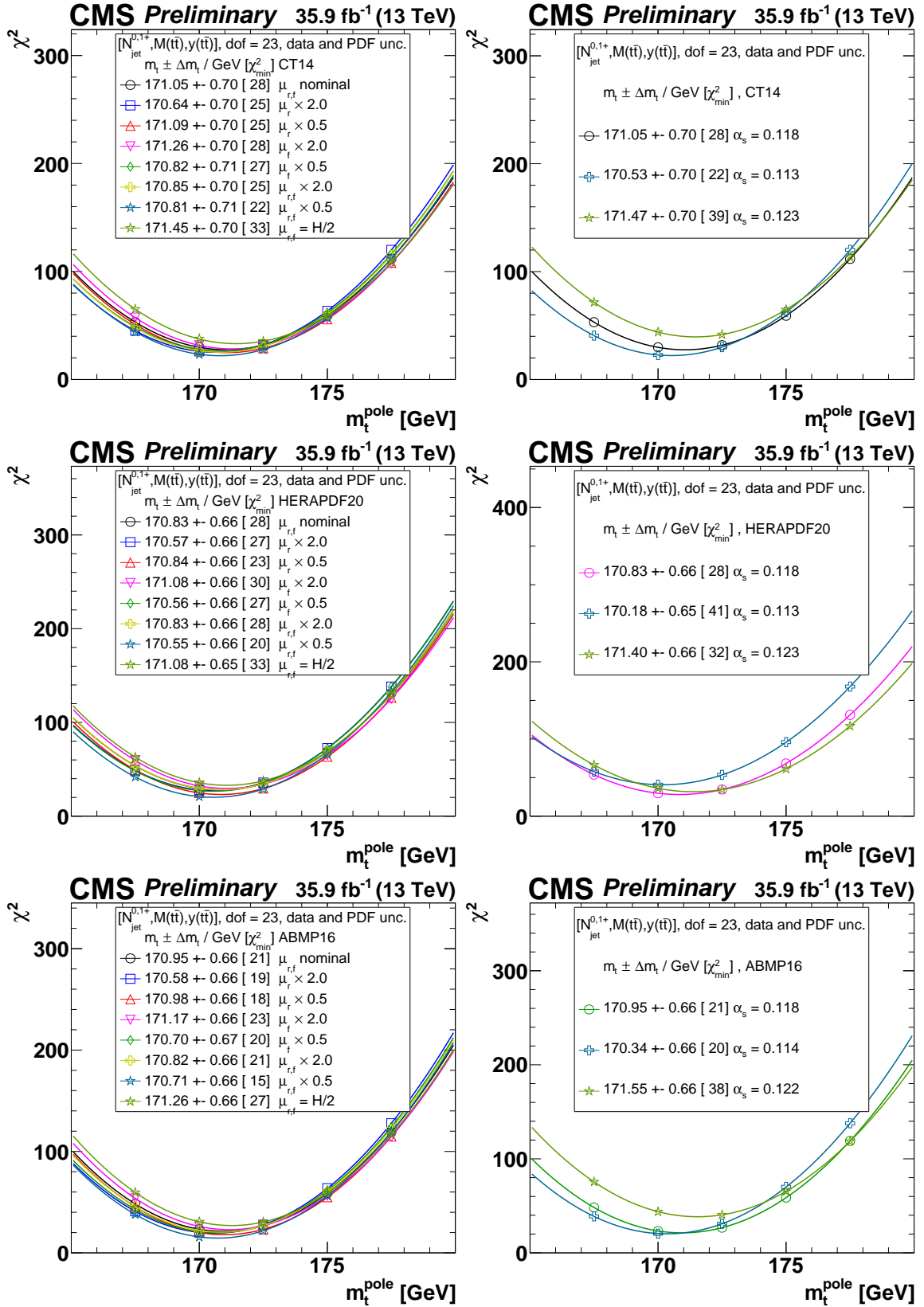


Figure 26: The  $m_t^{\text{pole}}$  extraction from the measured  $[N_{\text{jet}}^{0,1+}, M(t\bar{t}), y(t\bar{t})]$  cross sections using varied scale and  $\alpha_s$  settings and CT14 (top), HERAPDF2.0 (middle) and ABMP16 (bottom) PDF sets. Details can be found in the caption of Fig. 17.

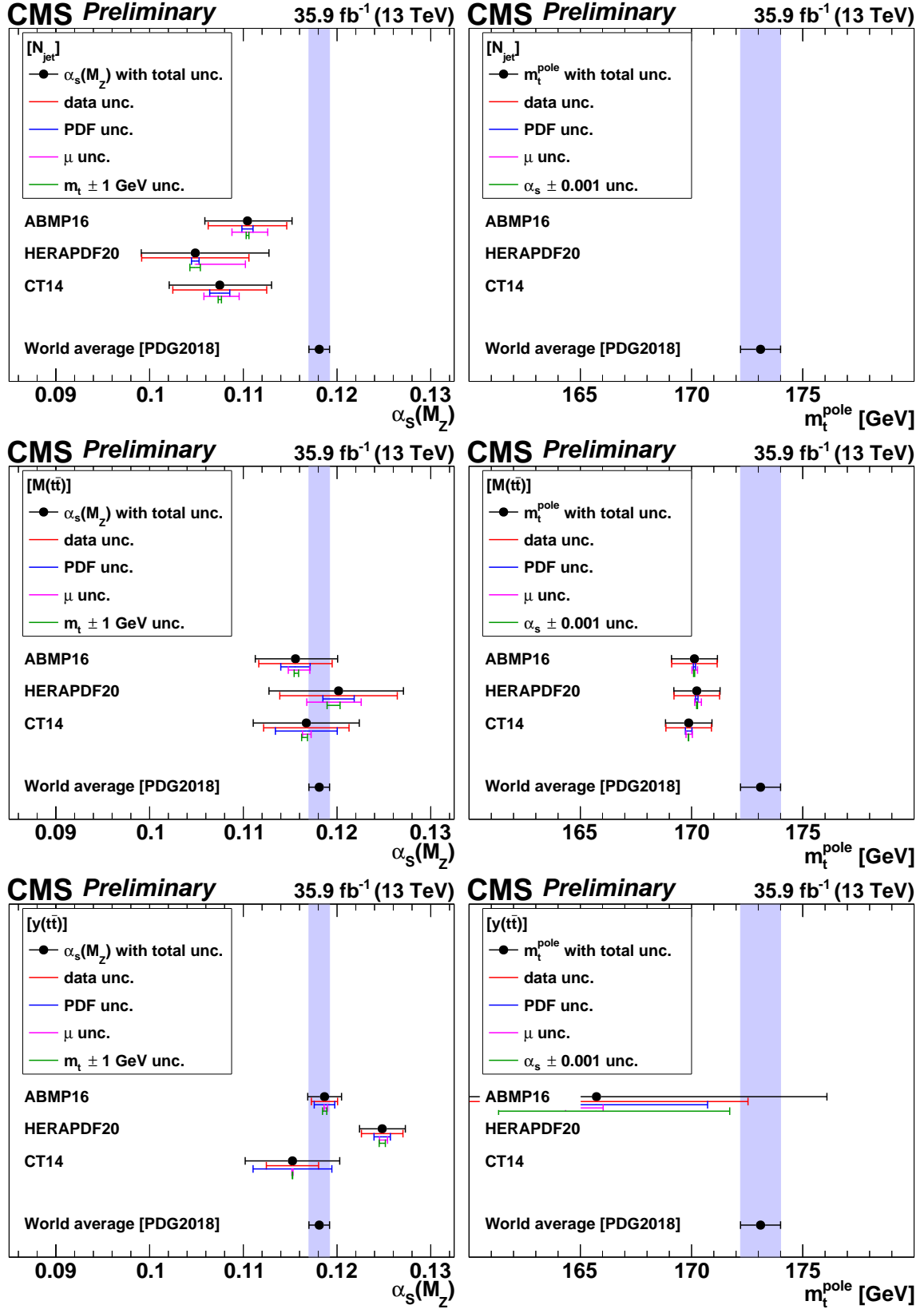


Figure 27: The  $\alpha_s$  and  $m_t^{\text{pole}}$  values extracted using different single-differential cross sections. For central values outside the displayed  $m_t^{\text{pole}}$  range, no result is shown. Details can be found in the caption of Fig. 18.



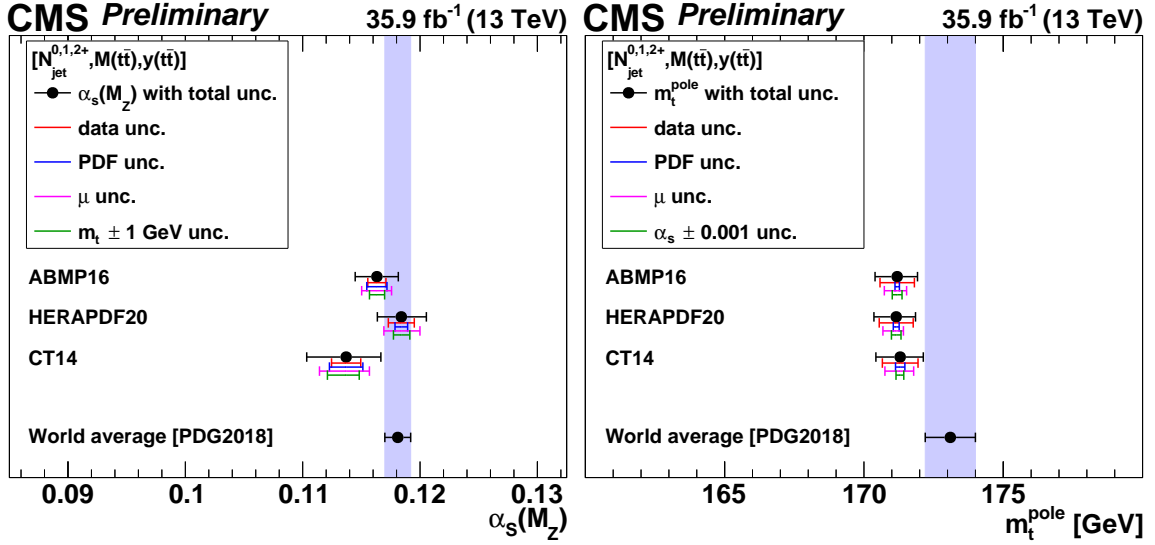


Figure 28: The  $\alpha_s$  (left) and  $m_t^{\text{pole}}$  (right) values extracted from the triple-differential  $[N_{\text{jet}}^{0,1,2+}, M(t\bar{t}), y(t\bar{t})]$  cross sections. Details can be found in the caption of Fig. 18.

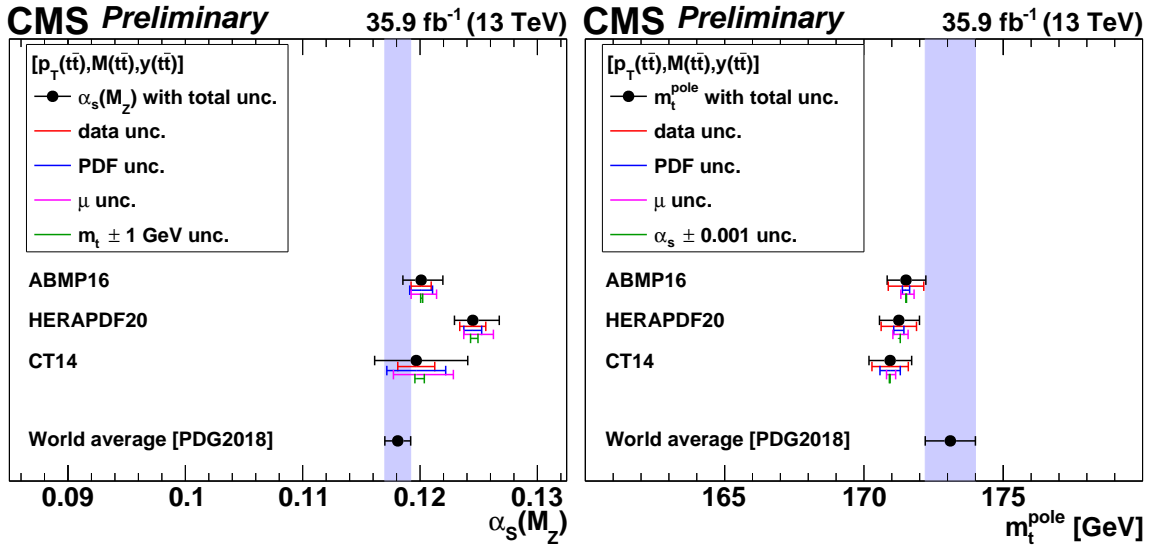


Figure 29: The  $\alpha_s$  (left) and  $m_t^{\text{pole}}$  (right) values extracted from the triple-differential  $[p_T(t\bar{t}), M(t\bar{t}), y(t\bar{t})]$  cross sections. Details can be found in the caption of Fig. 18.

are shown in Fig. 29. They are consistent with the nominal ones (see Fig. 18) but have slightly larger uncertainties. The experimental, PDF and scale uncertainty components are increased compared to the nominal results using the  $[N_{\text{jet}}^{0,1+}, M(t\bar{t}), y(t\bar{t})]$  cross sections. Nevertheless, these results present an important cross check, because the  $[p_T(t\bar{t}), M(t\bar{t}), y(t\bar{t})]$  cross sections are provided at parton level and do not require non-perturbative corrections, which have to be applied for distributions involving  $N_{\text{jet}}$ .